Atmospheric
Chemistry
and Physics

Supplement of

A machine learning examination of hydroxyl radical differences among model simulations for CCMI-1

Julie M. Nicely et al.

Correspondence to: Julie M. Nicely (julie.m.nicely@nasa.gov)

Text S1

Here we present and discuss our analysis of the REF-C1 historical free-running simulations from CCMI. These simulations differ from those presented in the main body of the text in that the models do not constrain their meteorological fields in any way to historical meteorology. Winds, temperature, pressure, and water vapor are internally calculated by the Chemistry Climate Models (CCMs), so it is unlikely that meteorological features, such as ENSO and drought-induced biomass burning, align with reality.

The CCMs that provided REF-C1 simulations, including all output necessary to perform the same NN training and inter-model comparison described in the main text (Sections 3.1 and 3.2), are: ACCESS-CCM, CAM4-Chem, EMAC-L47MA, EMAC-L90MA, GEOSCCM, MOCAGE, MRI-ESM1r1, NIWA-UKCA, SOCOL3, ULAQ-CCM, and WACCM. Details of the REF-C1 simulation, performed for 1960-2010, are found in Hegglin & Lamarque (2015) and Morgenstern et al. (2017). One model, the Coupled Model (CM3) developed at the Geophysical Fluid Dynamics Laboratory (GFDL) (Donner et al., 2011) is added to the free-running analysis. The simulation of the CM3 model used here is a 400-year time-slice run, with perpetual emissions representative of year 2000 (Westervelt et al., 2018). Further details of the model setup are available in Westervelt et al. (2017). By including CM3 with the group of REF-C1 CCMI models, we analyse a total of 12 free-running models.

The inter-model comparison conducted for the REF-C1 model simulations was performed following the same protocol as described in Section 3.2 of the main text. The values of τ_{CH_4} calculated for each month of year 2000 are shown in Figure S26, while the annual average changes in τ_{CH_4} ($\Delta\tau_{CH_4}$) by model, for NN swaps of the indicated species, are shown in Figure S27. Overall, values of $\Delta\tau_{CH4}$ are larger than the same values calculated for the REF-C1SD specified dynamics simulations examined in the main text, and chemical mechanism differences appear to play a larger role. For example, the variables responsible for the largest OH differences are O_3 in the free-running simulations and JO^1D in the specified dynamics simulations (Fig. 5). The mean absolute value of the annual average $\Delta\tau_{CH4}$ due to O_3 in the free-running models is 0.60$\pm$0.69 years, while the same aggregation of $\Delta\tau_{CH4}$ values due to JO^1D in the specified dynamics models is 0.54$\pm$0.57 years. The second-most important variables, NO_x in the free-running simulations and O_3 in the specified dynamics simulations, yield $\Delta\tau_{CH4}$ values of, on average, 0.48$\pm$1.11 years and 0.42$\pm$0.49 years, respectively. The remainder $\Delta\tau_{CH4}$ attributed to chemical mechanism differences between models averages to 0.69$\pm$1.14 years in the free-running simulations as opposed to 0.36$\pm$0.46 years in the specified dynamics simulations.

The larger values of $\Delta\tau_{CH4}$ in the free-running models may convey that meteorological differences are imparting an impact on OH through mechanisms that are not sufficiently represented in the input variables chosen for the NN analysis. It is possible that other chemical species not included here that are substantially altered by meteorology or transport and in turn alter OH concentrations would manifest as larger values of $\Delta\tau_{CH4}$, particularly in the Mech. term. On the other hand, if those missing species are correlated with one of the species or variables used as an input to the NN, the $\Delta\tau_{CH4}$ attributed to that input may also be inflated. As a result, we caution that model variations in meteorological conditions, expected as a result of their free-running setup in the REF-C1 simulation, could generate artifacts that are less likely to arise in the REF-C1SD simulation comparison, in which temperatures, transport, cloud cover, and water vapor should be reasonably similar.

As with the inter-model comparison of the specified dynamics simulations, results of the free-running model analysis exhibit a multitude of interesting features. While we cannot explore each one with the amount of attention it is due, we would like to

discuss one example that highlights the utility of the NN method. In Fig. S27, the $\Delta\tau_{CH4}$ attributed to JNO_2 shows curious behavior for the SOCOL3 model. The absence of spread about the mean value of $\Delta\tau_{CH4}$ is highly unusual, except for instances where a model shows no or very little response of OH to a NN input. The relatively large value of $\Delta\tau_{CH4}$ for SOCOL3 ($+0.69\pm0.09$ years) paired with the small variation in this quantity across all the model pairings most likely indicates an issue in the model. Figure S28 shows the JNO_2 fields, taken directly from each CCM for January, 2000, at 850 hPa. There is much diversity in this quantity across all the models, but the SOCOL3 model exhibits markedly high values, within the tropics especially. Revell et al. (2018) also identify this issue and suggest that the treatment of solar backscatter from clouds may be responsible for biases in the photolysis look-up table calculations. Additionally, a geometric spatial pattern is evident between the latitudes 0° and 30°S, which is unlikely to result from any physical process in the true atmosphere. This may indicate a problem in the way time averaging is conducted to achieve the monthly mean fields reported, a dependence within the photolysis code on a non-continuous time variable (since the pattern repeats regularly every 30° of longitude), or a similar issue. To reduce the likelihood of a bias due to differences in the way that monthly means are calculated, it may be useful for future inter-model comparison efforts to clearly define a desired method of averaging (e.g., composing daily averages from hourly output then averaging the daily means as opposed to averaging a month's worth of 6-hourly instantaneous output). It is of course possible to identify this variety of idiosyncrasy by careful inspection of each model field that is output from a model, but that is a time- and labor-intensive task. Instead, the NN method is capable of pointing a user directly to the offending fields, at least for the variables that are of sufficient relevance to OH chemistry that we have included them here as inputs. In the case that a user wants simply to detect outlier model fields as in this case, it is entirely feasible that the NN method could be adapted for that purpose.

References

Donner, L. J., Wyman, B. L., Hemler, R. S., Horowitz, L. W., Ming, Y., Zhao, M., Golaz, J. C., Ginoux, P., Lin, S. J., Schwarzkopf, M. D., Austin, J., Alaka, G., Cooke, W. F., Delworth, T. L., Freidenreich, S. M., Gordon, C. T., Griffies, S. M., Held, I. M., Hurlin, W. J., Klein, S. A., Knutson, T. R., Langenhorst, A. R., Lee, H. C., Lin, Y., Magi, B. I., Malyshev, S. L., Milly, P. C. D., Naik, V., Nath, M. J., Pincus, R., Ploshay, J. J., Ramaswamy, V., Seman, C. J., Shevliakova, E., Sirutis, J. J., Stern, W. F., Stouffer, R. J., Wilson, R. J., Winton, M., Wittenberg, A. T. and Zeng, F.: The dynamical core, physical parameterizations, and basic simulation characteristics of the atmospheric component AM3 of the GFDL global coupled model CM3, J. Clim., 24(13), 3484–3519, doi:10.1175/2011JCLI3955.1, 2011.

Hegglin, M. I. and Lamarque, J. F.: The IGAC/SPARC Chemistry-Climate Model Initiative Phase-1 (CCMI-1) model data output, NCAS Br. Atmos. Data Cent. [online] Available from: http://catalogue.ceda.ac.uk/uuid/9cc6b94df0f4469d8066d69b5df879d5 (Accessed 16 July 2019), 2015.

Morgenstern, O., Hegglin, M., Rozanov, E., O'Connor, F., Luke Abraham, N., Akiyoshi, H., Archibald, A., Bekki, S., Butchart, N., Chipperfield, M., Deushi, M., Dhomse, S., Garcia, R., Hardiman, S., Horowitz, L., Jöckel, P., Josse, B., Kinnison, D., Lin, M., Mancini, E., Manyin, M., Marchand, M., Marécal, V., Michou, M., Oman, L., Pitari, G., Plummer, D., Revell, L., Saint-Martin, D., Schofield, R., Stenke, A., Stone, K., Sudo, K., Tanaka, T., Tilmes, S., Yamashita, Y., Yoshida, K. and Zeng, G.: Review of the global models used within phase 1 of the Chemistry-Climate Model Initiative (CCMI), Geosci. Model Dev., 10(2), 639–671, doi:10.5194/gmd-10-639-2017, 2017.

Revell, L. E., Stenke, A., Tummon, F., Feinberg, A., Rozanov, E., Peter, T., Abraham, N. L., Akiyoshi, H., Archibald, A. T., Butchart, N., Deushi, M., Jöckel, P., Kinnison, D., Michou, M., Morgenstern, O., O&apos;Connor, F. M., Oman, L. D., Pitari, G., Plummer, D. A., Schofield, R., Stone, K., Tilmes, S., Visioni, D., Yamashita, Y. and Zeng, G.: Tropospheric ozone in CCMI models and Gaussian process emulation to understand biases in the SOCOLv3 chemistry–climate model, Atmos. Chem. Phys., 18(21), 16155–16172, doi:10.5194/acp-18-16155-2018, 2018.

Westervelt, D. M., Conley, A. J., Fiore, A. M., Lamarque, J.-F., Shindell, D., Previdi, M., Faluvegi, G., Correa, G. and Horowitz, L. W.: Multimodel precipitation responses to removal of U.S. sulfur dioxide emissions, J. Geophys. Res. Atmos., 122(9), 5024–5038, doi:10.1002/2017JD026756, 2017.

Westervelt, D. M., Conley, A. J., Fiore, A. M., Lamarque, J.-F., Shindell, D. T., Previdi, M., Mascioli, N. R., Faluvegi, G., Correa, G. and Horowitz, L. W.: Connecting regional aerosol emissions reductions to local and remote precipitation responses, Atmos. Chem. Phys., 18(16), 12461–12475, doi:10.5194/acp-18-12461-2018, 2018.

Table S1. The sample size, i.e., number of tropospheric model gridboxes, used for the training of each model's NN, for each month

Model	January	April	July	October
CAM4Chem	424,381	422,602	430,701	427,699
EMAC-L47MA	179,048	178,435	184,163	182,065
EMAC-L90MA	167,025	166,307	173,231	170,621
GEOS-Replay	396,694	395,066	401,571	398,479
GEOS-Chem	101,305	100,587	102,441	101,758
GMI	398,655	397,802	401,866	400,860
MOCAGE	427,194	426,621	430,437	432,303
MRI-ESM1r1	270,651	267,521	284,988	273,127
OsloCTM	378,332	376,794	382,529	379,338
WACCM	424,298	422,580	430,601	427,766

Table S2. Constrained meteorology (REF-C1SD) CCMI model neural network training statistics, including mean squared error with regularization (MSE_REG), mean squared error (MSE), sum of squared errors (SSE) and Pearson correlation coefficient (R).

Model	Month	MSE_REG	MSE	SSE	R
CAM4Chem	1	0.37923	4.1261×10^{-4}	175.11	0.99985
	4	0.29407	2.1851×10^{-4}	92.341	0.99987
	7	0.10253	3.2249×10^{-4}	138.90	0.99991
	10	0.19263	2.5806×10^{-4}	110.37	0.99980
EMAC-L47MA	1	0.18339	6.7995×10^{-4}	121.74	0.99976
	4	0.18699	2.0219×10^{-4}	36.078	0.99986
	7	0.087789	3.4581×10^{-4}	63.685	0.99991
	10	0.17907	1.9427×10^{-4}	35.369	0.99983
EMAC-L90MA	1	0.35482	5.2862×10^{-4}	88.293	0.99981
	4	0.099595	2.0500×10^{-4}	34.093	0.99985
	7	0.080911	4.1468×10^{-4}	71.836	0.99989
	10	0.20788	1.7210×10^{-4}	29.364	0.99985
GEOS-Replay	1	0.20707	2.6069×10^{-4}	103.41	0.99990
	4	0.18929	1.2464×10^{-4}	49.240	0.99991
	7	0.080128	2.8015×10^{-4}	112.50	0.99992
	10	0.22672	1.5059×10^{-4}	60.009	0.99988
GEOSChem	1	0.22284	1.5205×10^{-4}	15.404	0.99993
	4	0.061255	1.1911×10^{-4}	11.981	0.99994
	7	0.14682	1.3059×10^{-4}	13.378	0.99997
	10	0.14627	1.0033×10^{-4}	10.210	0.99993
GMI	1	0.074667	4.8862×10^{-4}	194.79	0.99980
	4	0.094182	1.8318×10^{-4}	72.869	0.99987
	7	0.11295	3.1920×10^{-4}	128.27	0.99990
	10	0.14209	2.0734×10^{-4}	83.115	0.99984
MOCAGE	1	0.71640	9.0308×10^{-4}	385.79	0.99969
	4	0.48984	5.0834×10^{-4}	216.87	0.99961
	7	0.34163	8.6047×10^{-4}	370.38	0.99976
	10	0.31921	6.3376×10^{-4}	273.98	0.99944
MRI-ESM1r1	1	0.23535	5.9525×10^{-4}	161.10	0.99972
	4	0.10819	4.0592×10^{-4}	108.59	0.99975
	7	0.099627	6.2950×10^{-4}	179.40	0.99986
	10	0.14278	3.6378×10^{-4}	99.36	0.99971
OsloCTM	1	0.099237	7.7313×10^{-4}	292.50	0.99972
	4	0.19119	2.1283×10^{-4}	80.193	0.99986
	7	0.17034	4.0701×10^{-4}	155.69	0.99988
	10	0.16749	1.9759×10^{-4}	74.955	0.99984
WACCM	1	0.075339	5.1098×10^{-4}	216.81	0.99980
	4	0.23018	1.9571×10^{-4}	82.702	0.99986
	7	0.11848	2.4019×10^{-4}	103.43	0.99991
	10	0.087687	3.0286×10^{-4}	129.55	0.99974

**Table S3.** Free-running (REF-C1) CCMI model neural network training statistics, as in Table S2.

Model	Month	MSE_REG	MSE	SSE	R
ACCESS-CCM	1	0.11715	9.6330×10^{-4}	163.80	0.99968
	4	0.16688	2.3802×10^{-4}	40.386	0.99987
	7	0.19878	3.3644×10^{-4}	58.507	0.99991
	10	0.089005	3.6215×10^{-4}	62.611	0.99974
CAM4Chem	1	0.055129	6.6306×10^{-4}	127.79	0.99974
	4	0.11032	2.8507×10^{-4}	54.614	0.99980
	7	0.13067	3.8054×10^{-4}	75.732	0.99988
	10	0.12742	2.5473×10^{-4}	49.706	0.99978
CM3	1	0.11112	4.6630×10^{-4}	125.73	0.99980
	4	0.16528	1.8858×10^{-4}	50.816	0.99989
	7	0.026817	8.8304×10^{-4}	239.79	0.99980
	10	0.082181	3.2942×10^{-4}	91.146	0.99971
EMAC-L47MA	1	0.072276	9.2591×10^{-4}	171.04	0.99969
	4	0.086863	2.4612×10^{-4}	45.659	0.99983
	7	0.10271	4.7184×10^{-4}	90.056	0.99988
	10	0.11785	2.0844×10^{-4}	39.311	0.99982
EMAC-L90MA	1	0.16911	7.2262×10^{-4}	126.75	0.99976
	4	0.076460	2.3894×10^{-4}	42.177	0.99982
	7	0.081041	5.0940×10^{-4}	92.539	0.99988
	10	0.12357	2.2109×10^{-4}	39.097	0.99982
GEOSCCM	1	0.18199	3.9622×10^{-4}	158.05	0.99984
	4	0.064835	2.3637×10^{-4}	94.576	0.99984
	7	0.18798	3.2447×10^{-4}	130.95	0.99991
	10	0.11525	2.5013×10^{-4}	100.29	0.99982
MOCAGE	1	0.34317	1.3971×10^{-3}	617.16	0.99957
	4	0.70165	4.7860×10^{-4}	210.00	0.99963
	7	0.54001	9.6137×10^{-4}	431.00	0.99976
	10	0.31103	5.6591×10^{-4}	254.71	0.99938
MRI-ESM1r1	1	0.25895	6.1599×10^{-4}	166.11	0.99970
	4	0.20258	3.8259×10^{-4}	101.85	0.99977
	7	0.22064	4.3767×10^{-4}	121.15	0.99987
	10	0.24607	3.4118×10^{-4}	92.663	0.99971
NIWA-UKCA	1	0.065453	1.1373×10^{-3}	193.66	0.99959
	4	0.17948	2.5409×10^{-4}	43.007	0.99986
	7	0.13032	3.8962×10^{-4}	68.185	0.99989
	10	0.18349	2.9323×10^{-4}	50.539	0.99981
SOCOL3	1	0.10894	7.6744×10^{-4}	85.386	0.99940
	4	0.15187	1.6699×10^{-4}	18.597	0.99978
	7	0.16907	3.5237×10^{-4}	40.847	0.99985
	10	0.14254	2.4928×10^{-4}	28.546	0.99953
ULAQ-CCM	1	0.058951	2.7677×10^{-4}	12.950	0.99989
	4	0.047113	2.0840×10^{-4}	9.6693	0.99982
	7	0.057370	2.9026×10^{-4}	14.398	0.99990

|	10	0.065023	1.3451×10^{-4}	6.5473	0.99988
WACCM	1	0.050710	5.7059×10^{-4}	110.51	0.99975
	4	0.11753	1.9040×10^{-4}	36.453	0.99984
	7	0.053290	3.2026×10^{-4}	63.519	0.99988
	10	0.13621	2.3013×10^{-4}	44.987	0.99977
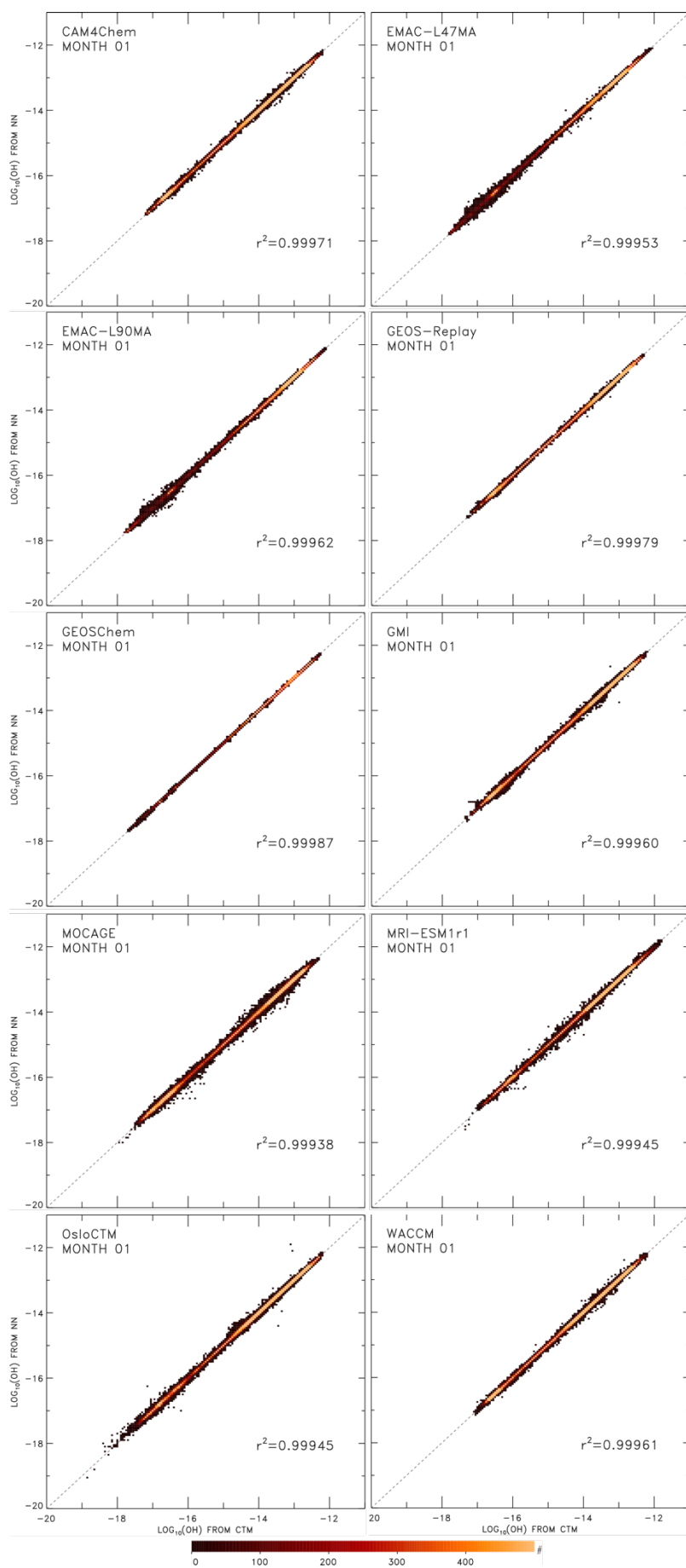
Figure S1. LOG$_{10}$ of OH mixing ratio calculated by NN versus that simulated by the native global model, for January. Colors indicate 2-D histogram to give indication of density of data points. All tropospheric model grid points are shown, including training, validation, and test data. Native model is indicated in the upper left corner of each panel, r^2 value is inscribed in the lower right, and 1:1 line is depicted as dashed grey line.
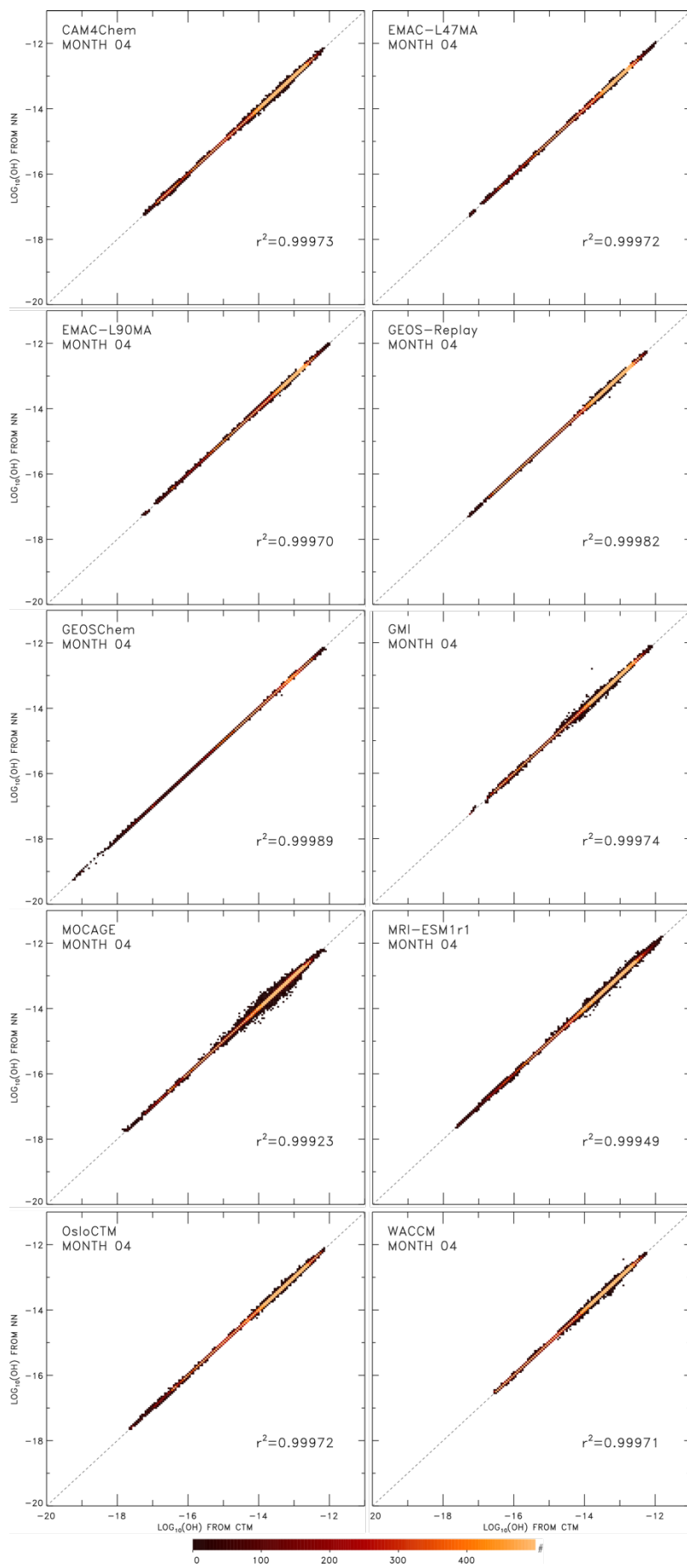
Figure S2. Same as Figure S1 except for month of April.
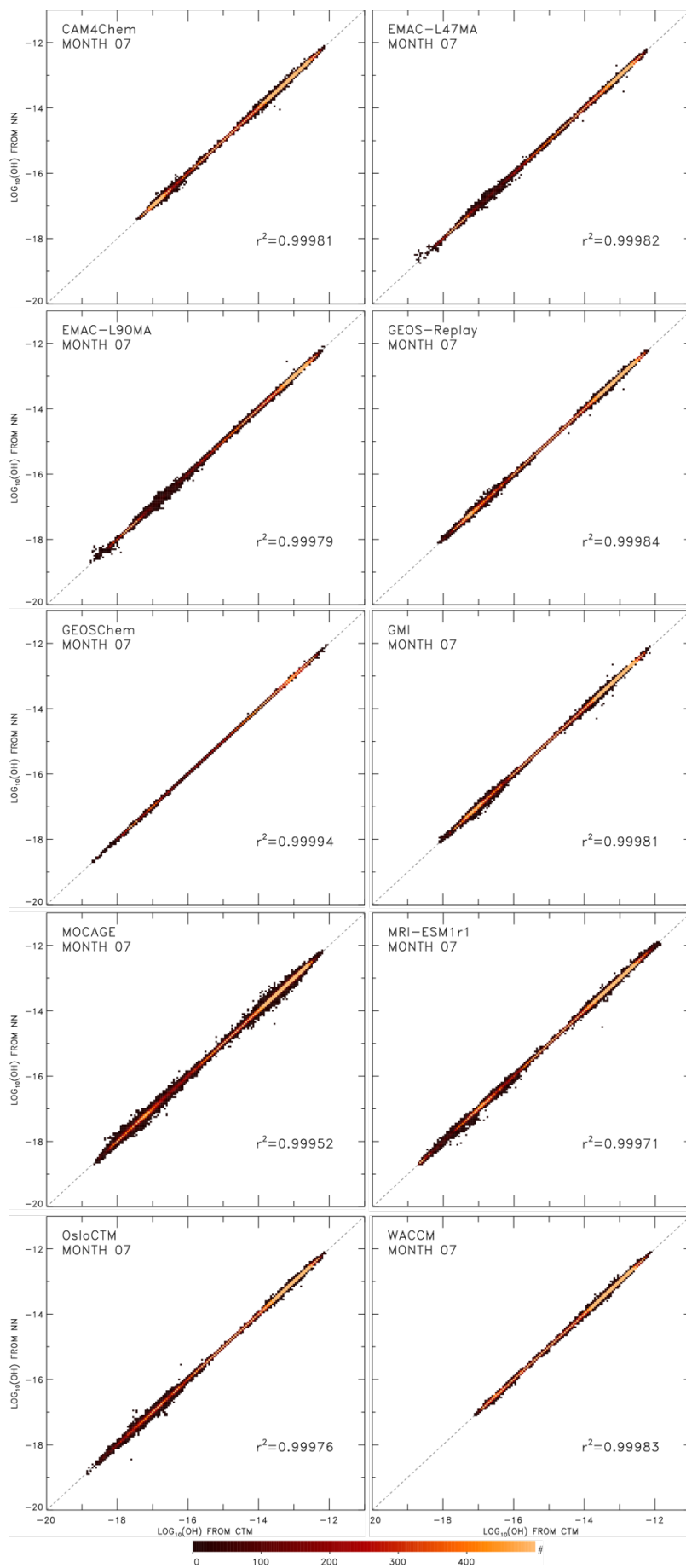
Figure S3. Same as Figure S1 except for month of July.
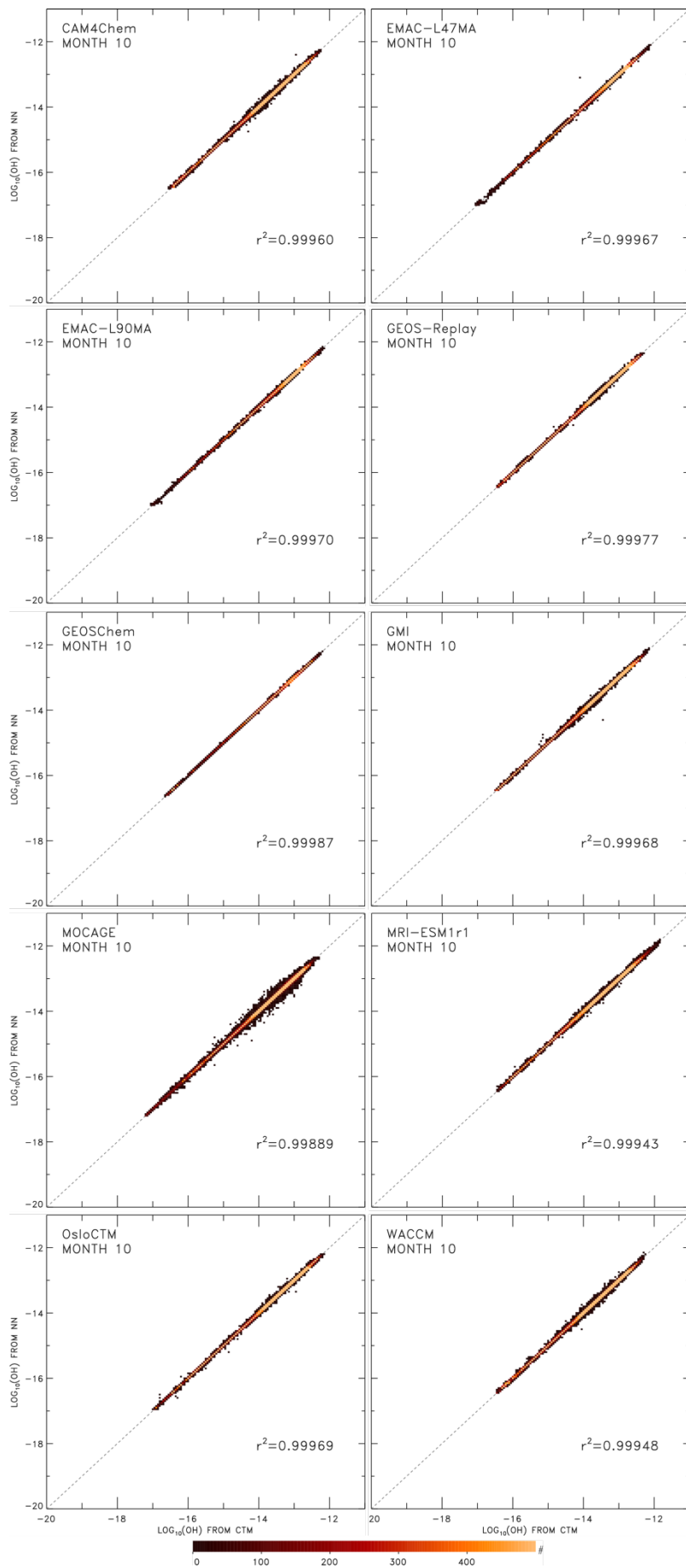
Figure S4. Same as Figure S1 except for month of October.
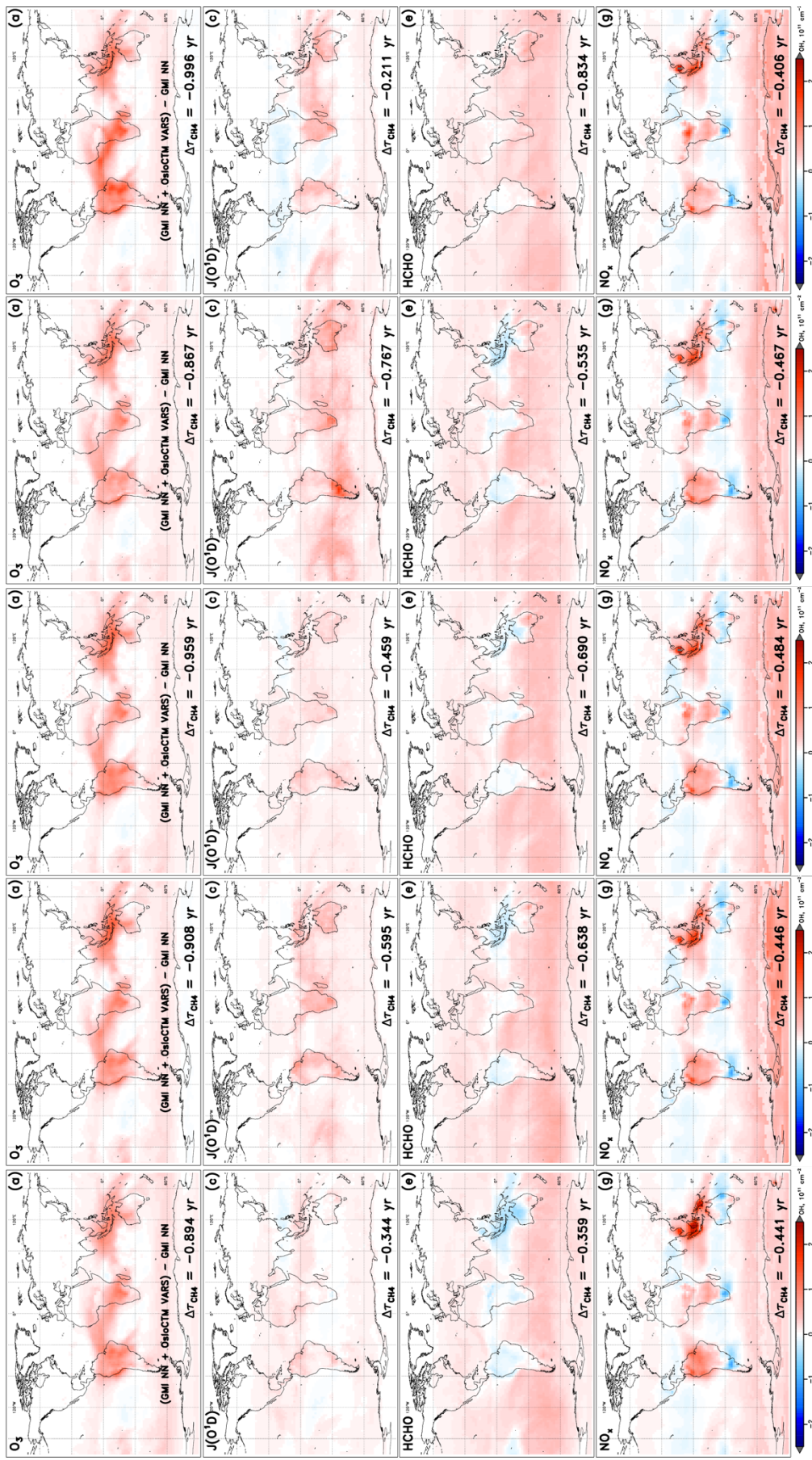
Figure S5. The equivalent of the left panels from Fig. 4 in the main text, evaluated for the other trainings of the January GMI NN. The second training (in the second column) produced the NN chosen for subsequent analysis. Training iteration is indicated by the column; the species swapped from the OsloCTM model into the GMI NN is indicated by the row (O_3, $J(O^1D)$, HCHO, and NO_x, from top to bottom).
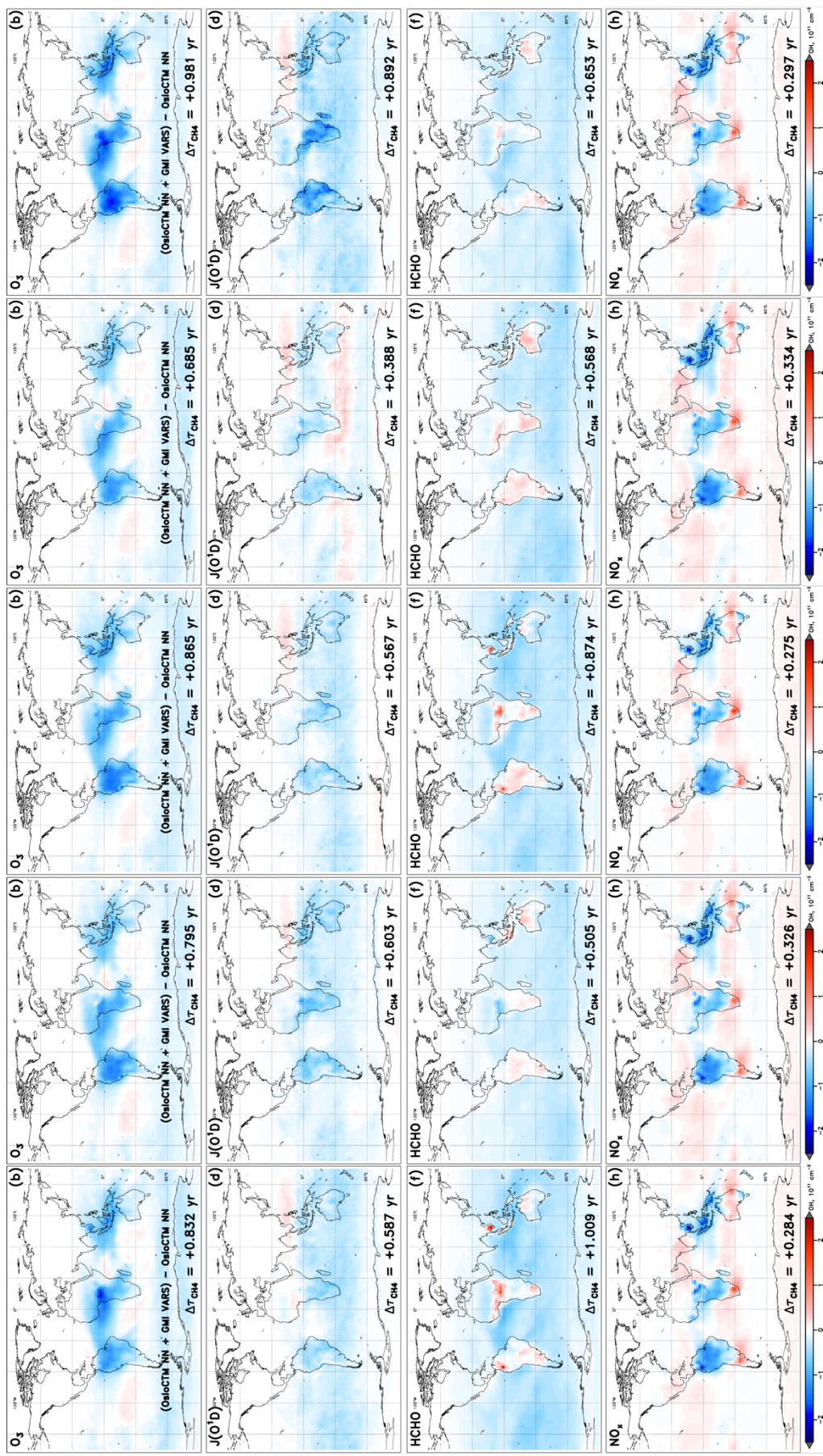
Figure S6. Same as Figure S5 except for the five trainings of the OsloCTM NN for January. The training instance for the January OsloCTM NN chosen for use in the broader analysis of this work was likewise the second, located in the second column.

Specified Dynamics, REF-C1SD

Free-running, REF-C1

$J(O^1D)_{SURF}/J(O^1D)_{UT}$

0.0   0.2   0.4   0.6   0.8   1.0
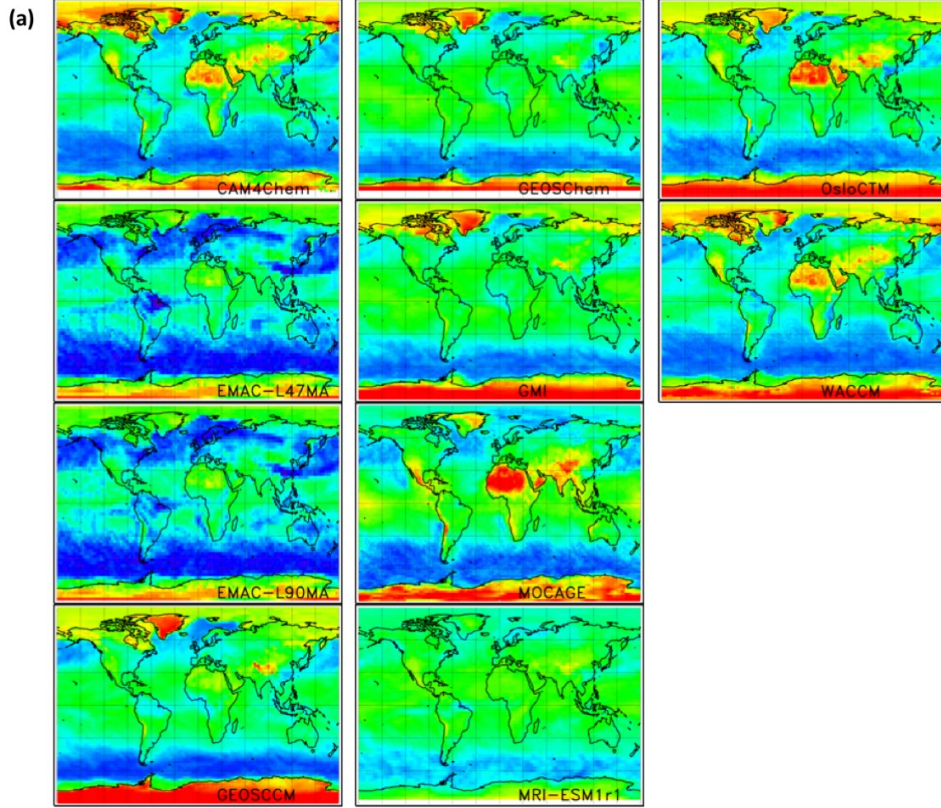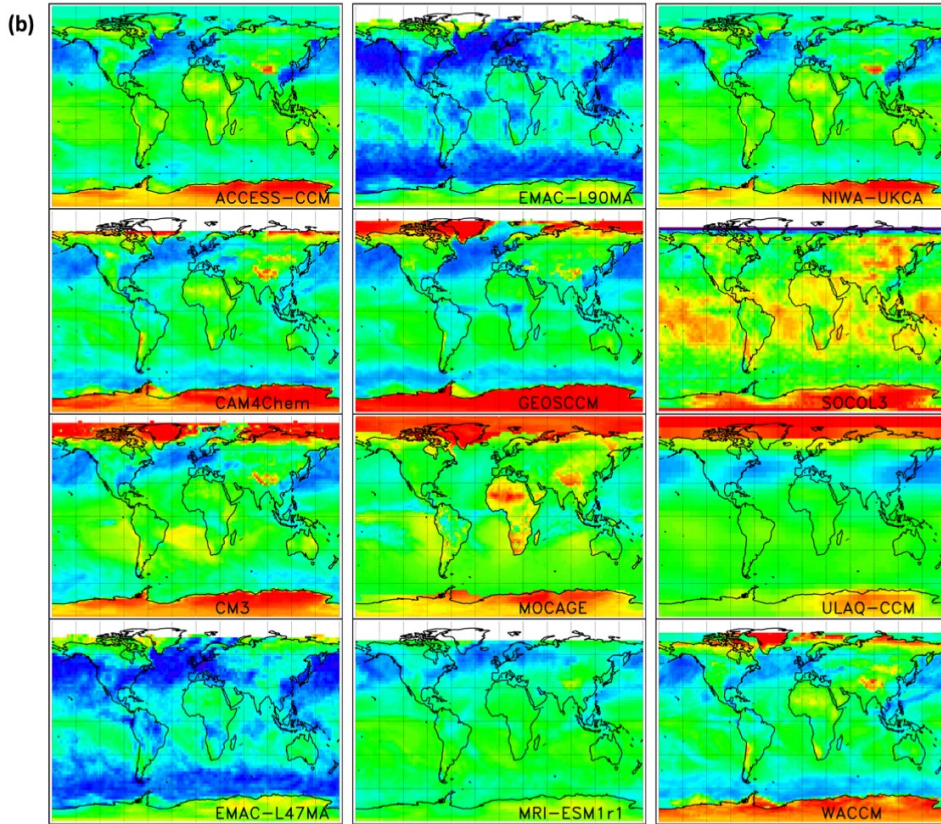
Figure S7. The ratio of JO^{1}D at the surface to JO^{1}D at the last pressure level within the troposphere before crossing the tropopause for the month in which each simulation set exhibited the largest τ_{CH4} differences attributed to JO^{1}D. (a) shows results from the REF-C1SD simulations for the month of April; (b) shows the REF-C1 simulations for the month of January. Suppression of this ratio below 1.0 is expected to result from cloud cover or other forms of absorption or scattering (by tropospheric O$_3$, aerosols, etc.).
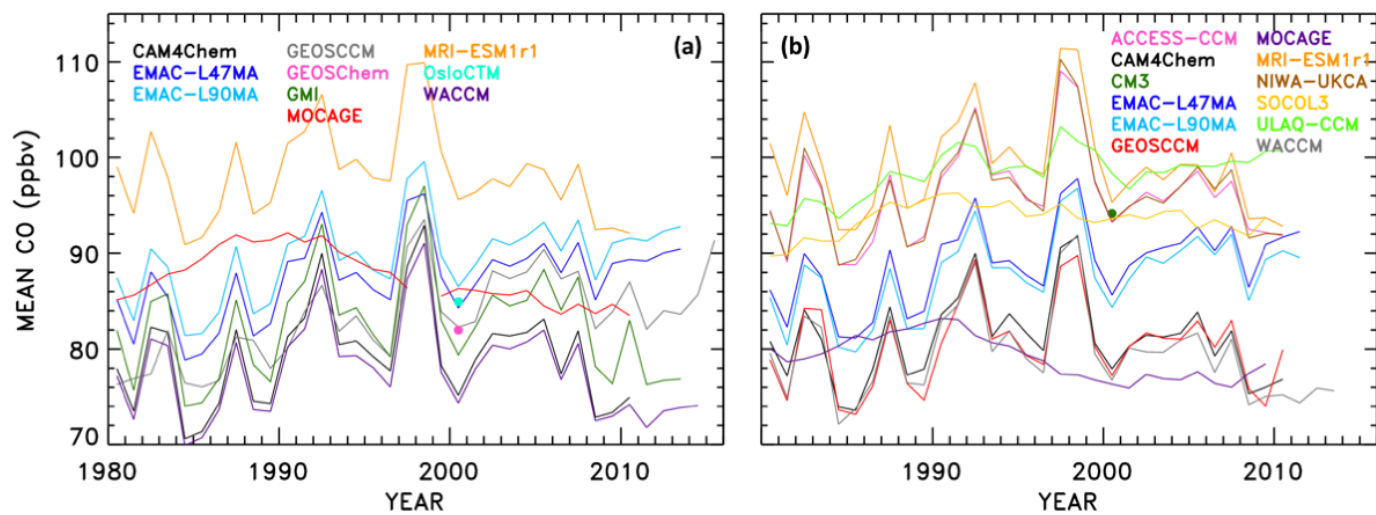
Figure S8. Time series of annually averaged CO mixing ratios at pressures greater than 700 hPa and latitudes between 30°S and 30°N from (a) the specified dynamics REF-C1SD simulations and (b) the free-running REF-C1 simulations.
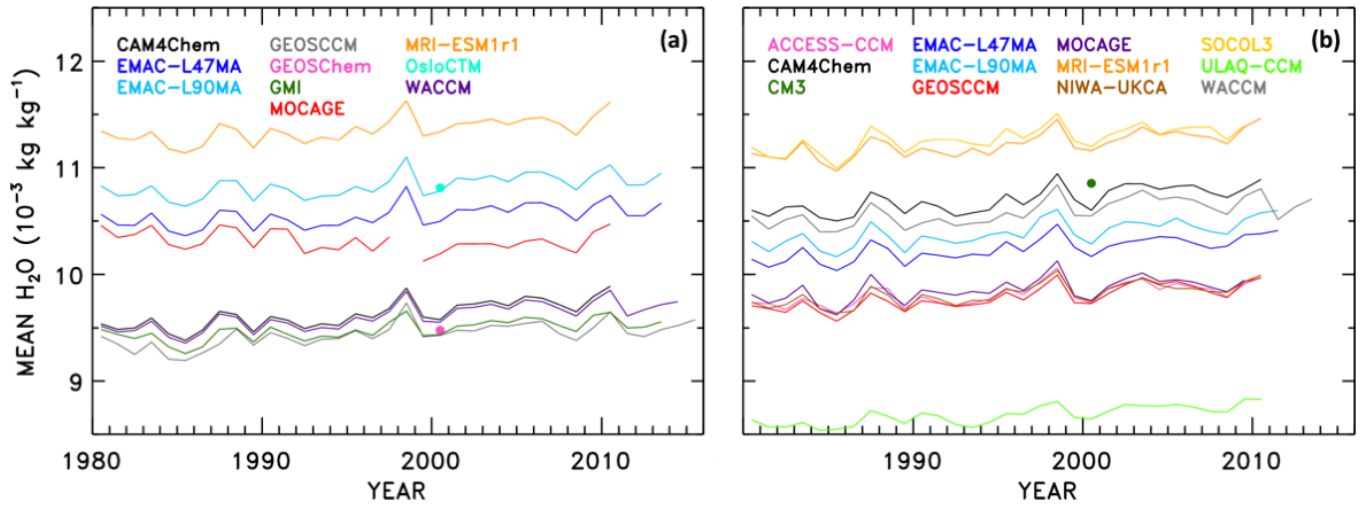
Figure S9. Time series of annually averaged H$_2$O mixing ratios at pressures greater than 700 hPa and latitudes between 30°S and 30°N from (a) the specified dynamics REF-C1SD simulations and (b) the free-running REF-C1 simulations.
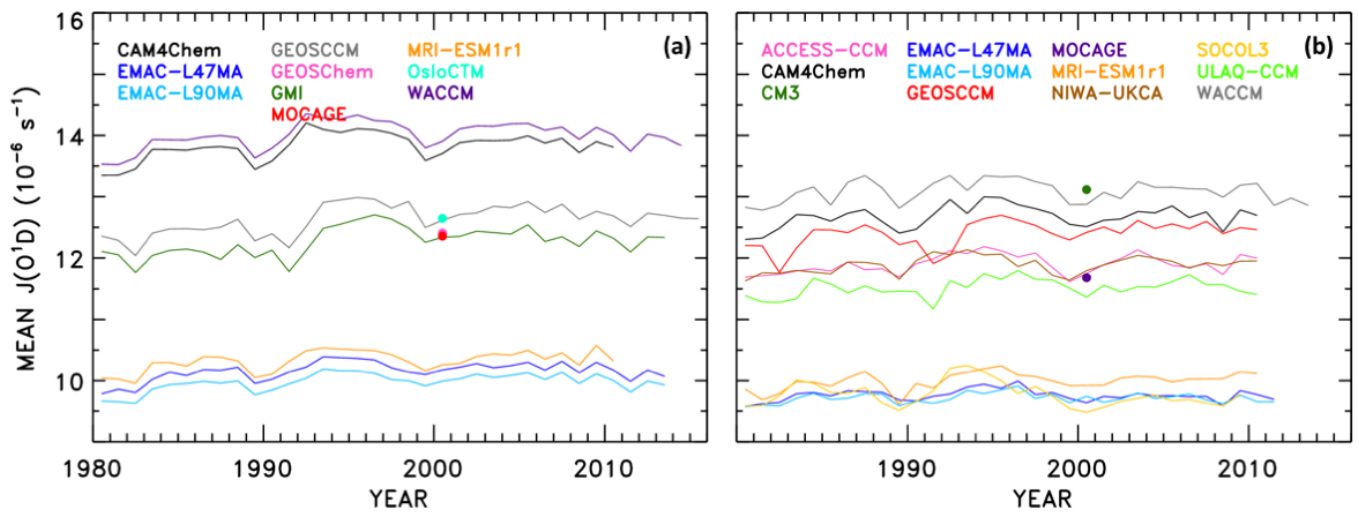
Figure S10. Time series of annually averaged J(O^{1}D) frequencies at pressures greater than 700 hPa and latitudes between 30°S and 30°N from (a) the specified dynamics REF-C1SD simulations and (b) the free-running REF-C1 simulations.
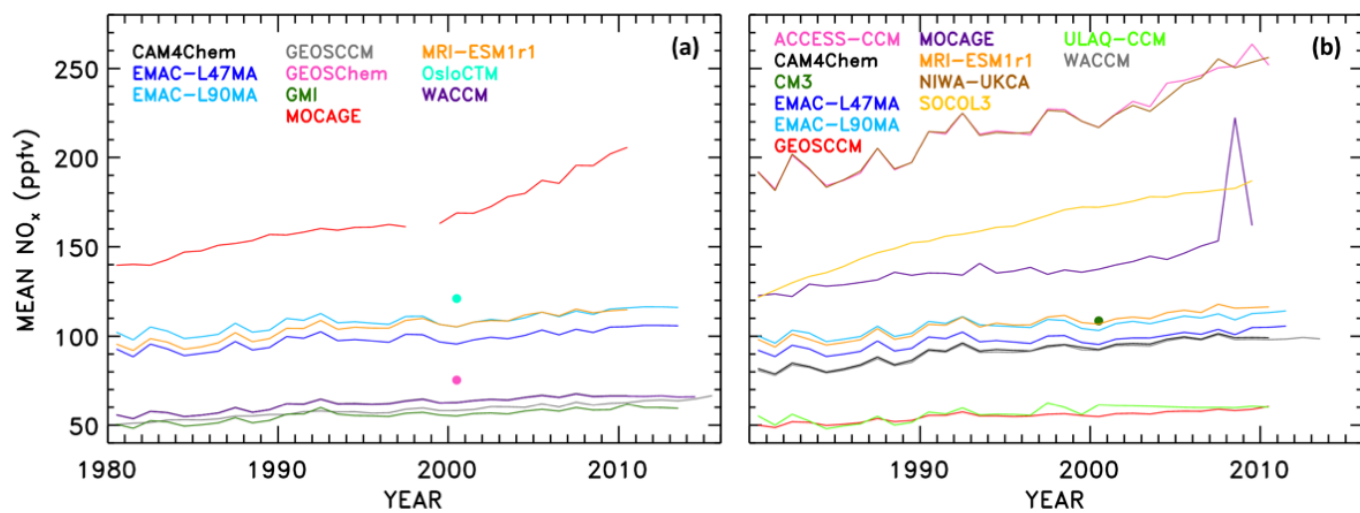
Figure S11. Time series of annually averaged NO$_x$ mixing ratios at pressures greater than 700 hPa and latitudes between 30°S and 30°N from (a) the specified dynamics REF-C1SD simulations and (b) the free-running REF-C1 simulations.
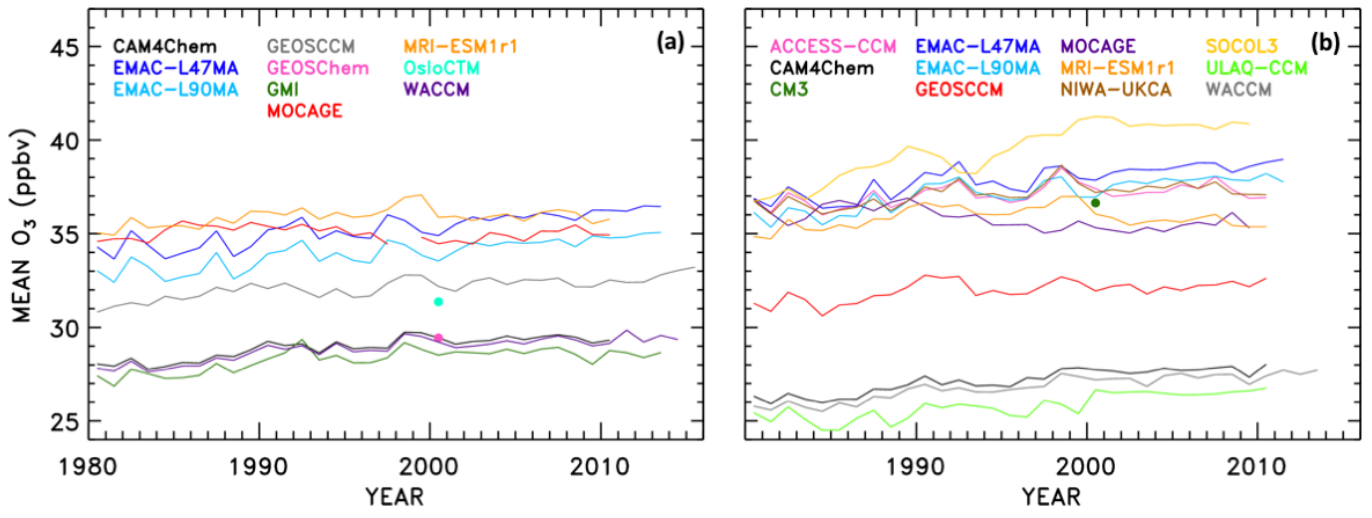
Figure S12. Time series of annually averaged O₃ mixing ratios at pressures greater than 700 hPa and latitudes between 30°S and 30°N from (a) the specified dynamics REF-C1SD simulations and (b) the free-running REF-C1 simulations.
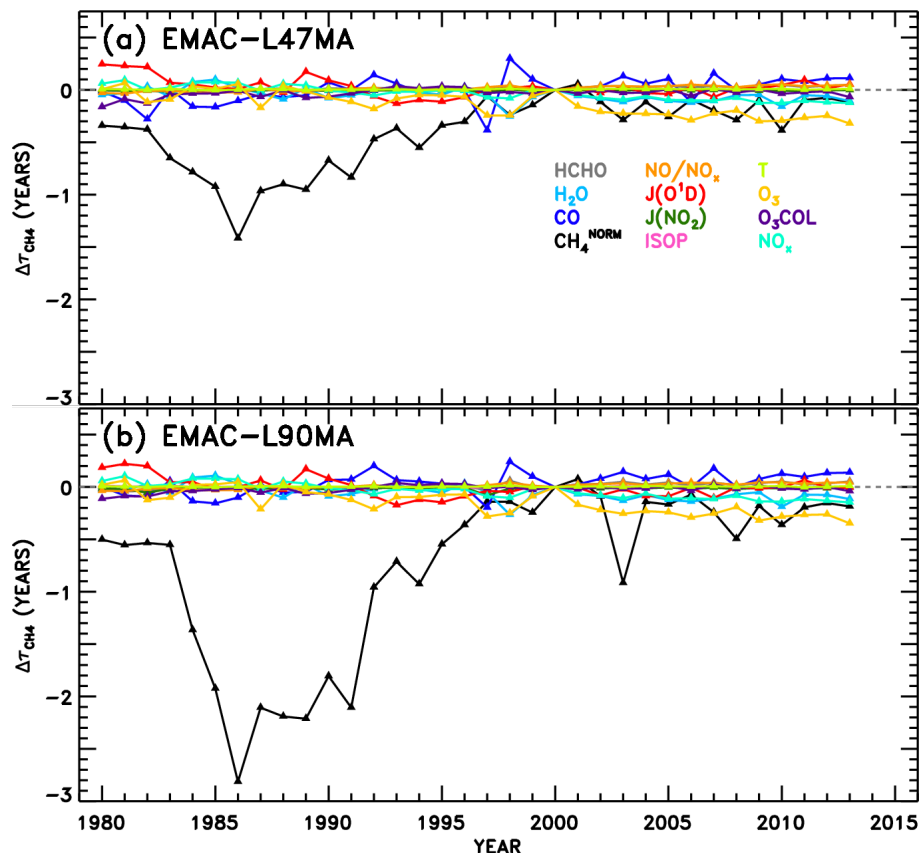
Figure S13. As in Figure 7 of the main text, panels (b) and (c), but with expanded y-axes to show the full range of the τ_{CH_4} responses to CH_4^{NORM} from the two EMAC model configurations.
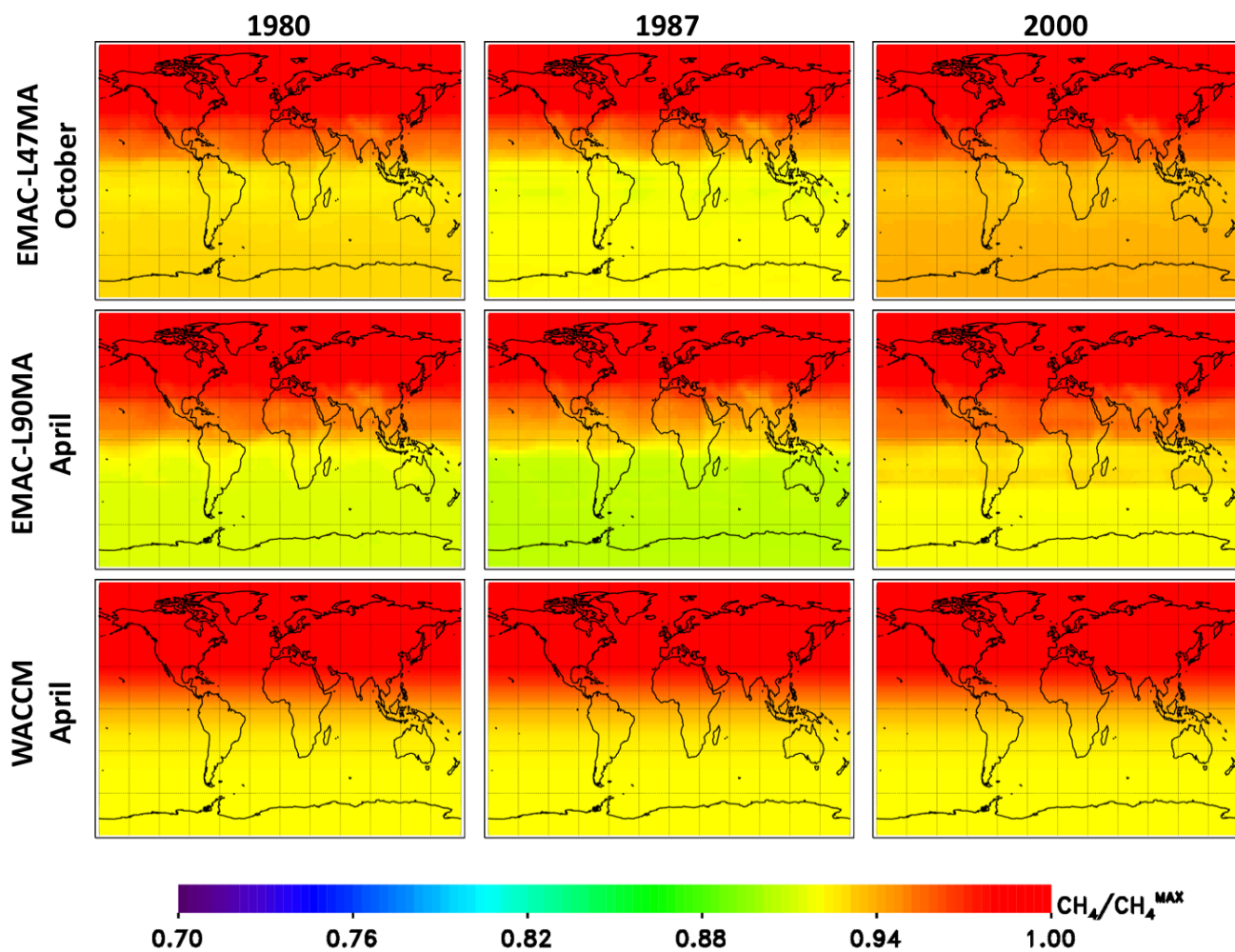
Figure S14. The ratio of local CH_4 mixing ratio to the maximum CH_4 mixing ratio found in the troposphere of a given model-simulated month, visualized for the pressure level nearest the surface, for the models, months, and years indicated. Results shown are for the REF-C1SD simulations. The normalized CH_4 quantity is used as an input to the neural networks to avoid issues introduced by non-overlapping fields of CH_4 absolute values between models and between years. This scaled CH_4 quantity is thus more accurately described as a measure of the CH_4 distribution within the troposphere. While the CH_4 distribution remains near-constant from year to year for a given month for most models (e.g., WACCM, bottom), the two configurations of the EMAC model show deviations from the trained (year 2000) distribution. Most notably between the mid-1980s and mid-1990s, CH_4 in the Southern Hemisphere decreases, relative to the higher CH_4 values in the Northern Hemisphere. It is these deviations in the EMAC CH_4 distributions that are likely driving the anomalous τ_{CH4} response in Fig. 7.
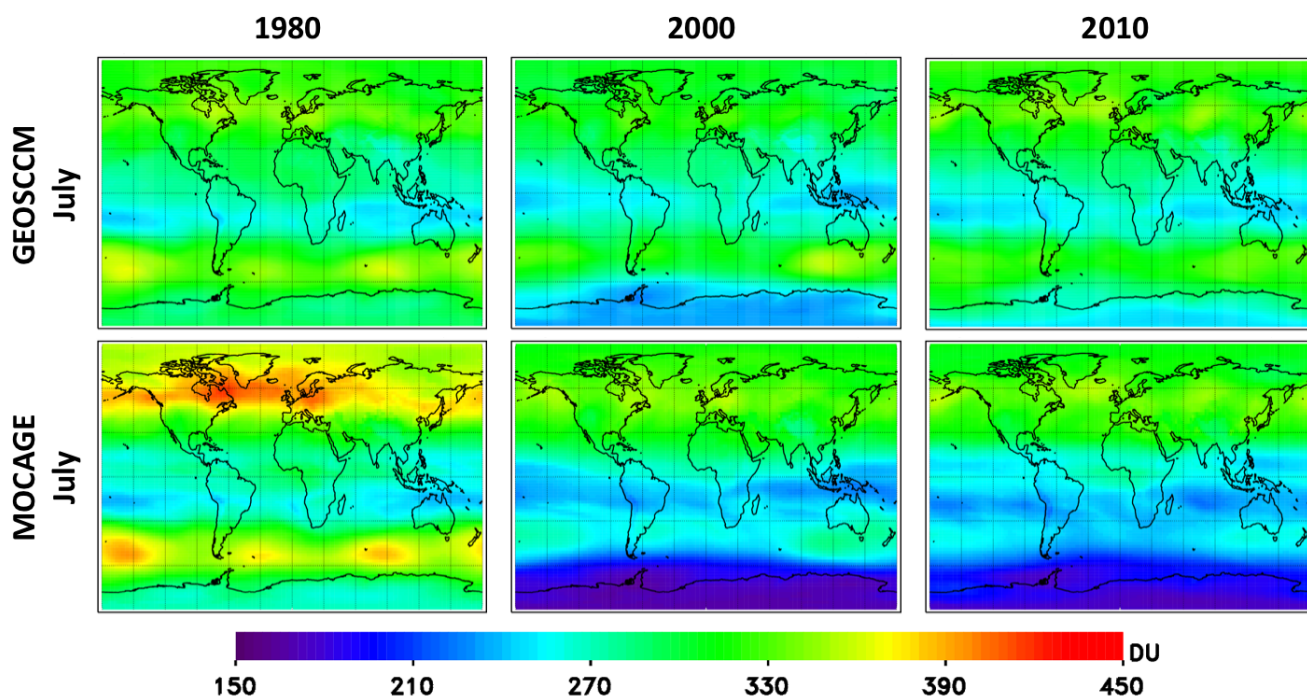
Figure S15. July total ozone columns from the GEOSCCM (top) and MOCAGE (bottom) REF-C1SD simulations for year 1980 (left), 2000 (center), and 2010 (right). While model differences between GEOSCCM and MOCAGE are apparent, it is the stark difference between year 1980 and 2000 in the MOCAGE model that is concerning and likely driving the anomalous τ_{CH4} response in the early- to mid-1980s, seen in Fig. 7. Other models, such as GEOSCCM, do not show such drastic differences between year 1980 and 2000 ozone column amounts.
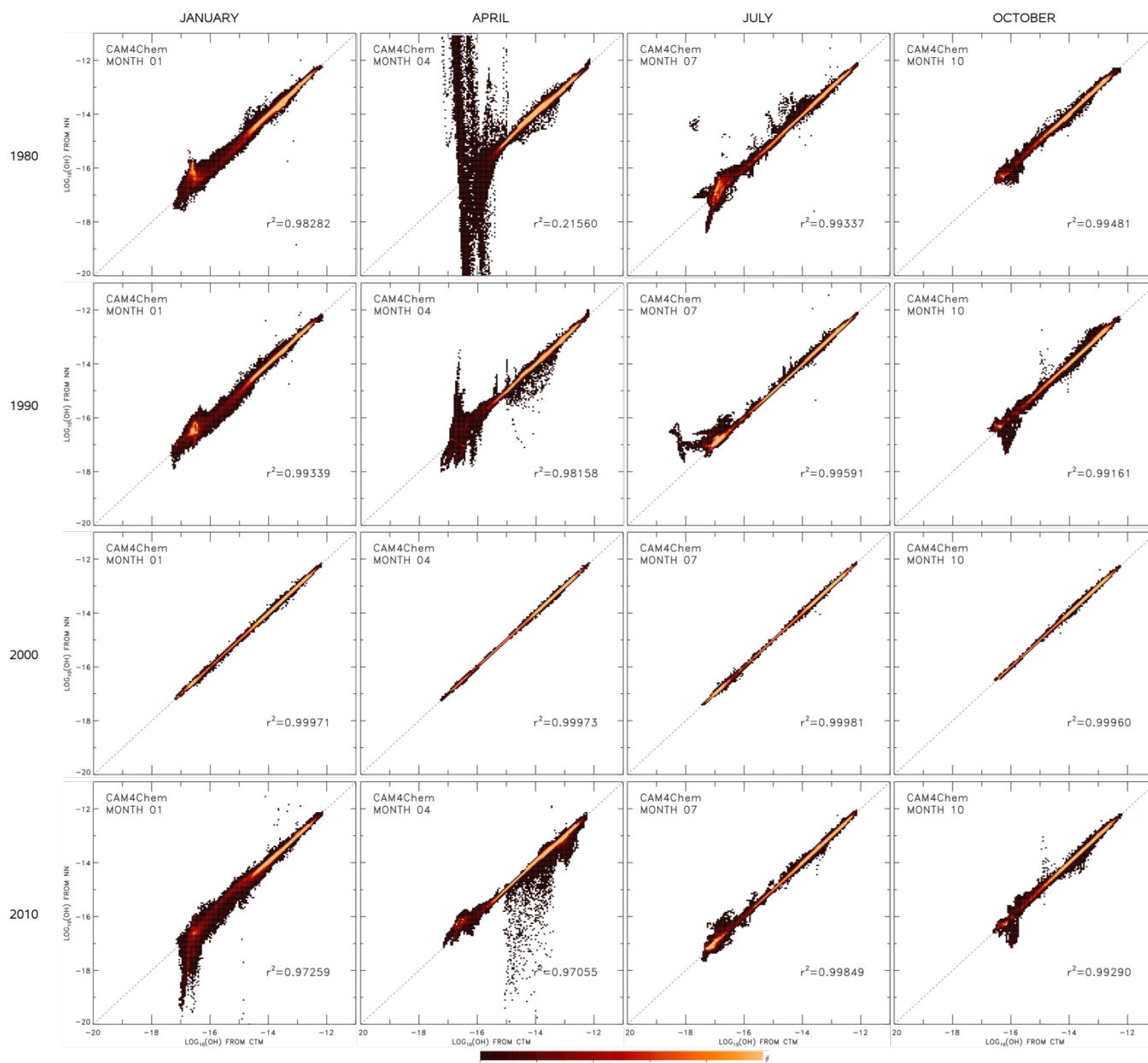
Figure S16. NN performance plots, as in Figure S1, but for only the REF-C1SD simulation of the CAM4-Chem model, evaluated for years 1980, 1990, 2000, and 2010 (from top to bottom). For each month (represented by the column), the same NN, trained on year 2000 model output, is subsequently run with inputs taken from the alternative years.
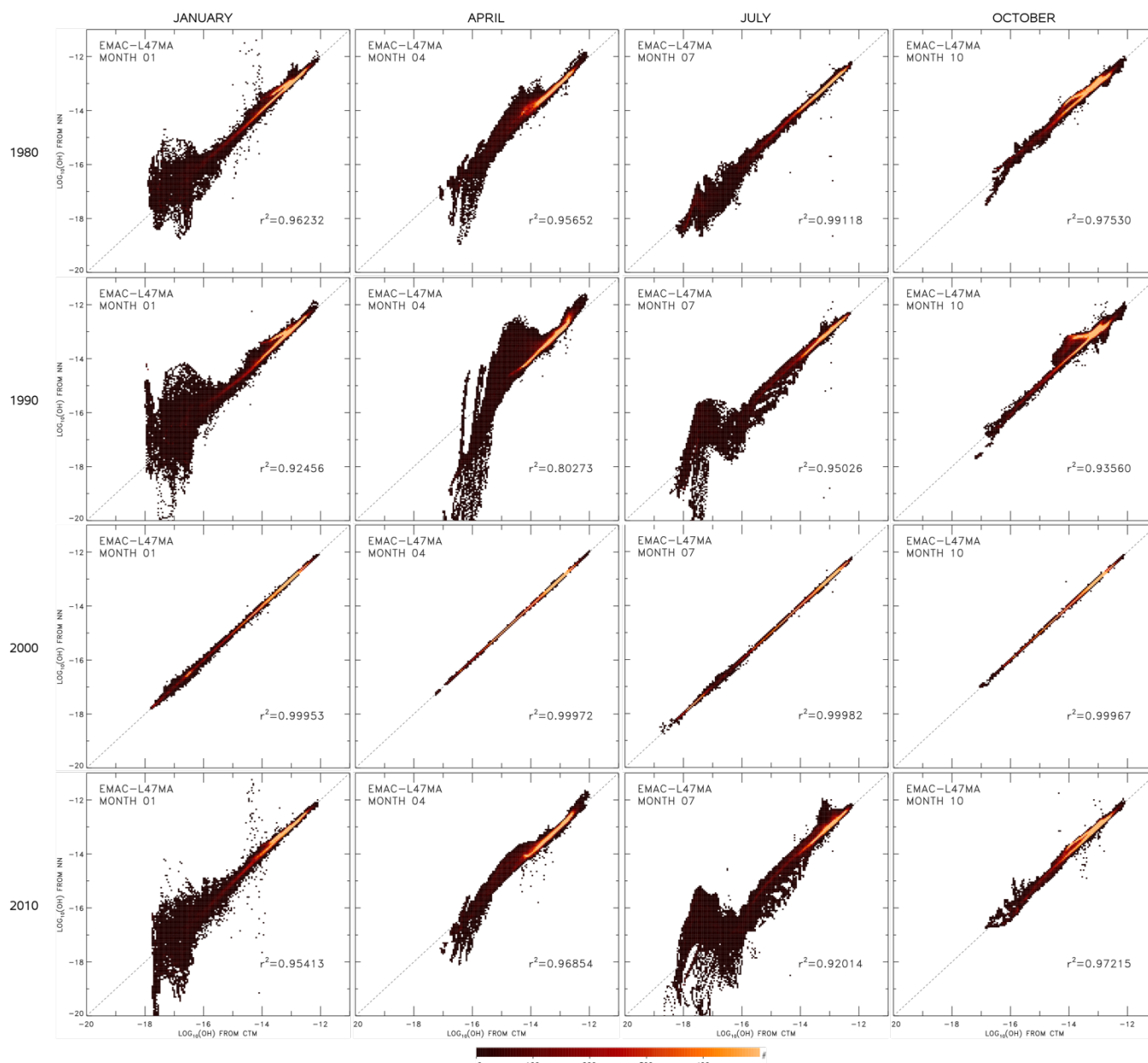
Figure S17. As in Figure S16, but for the REF-C1SD simulation of the EMAC-L47MA model.
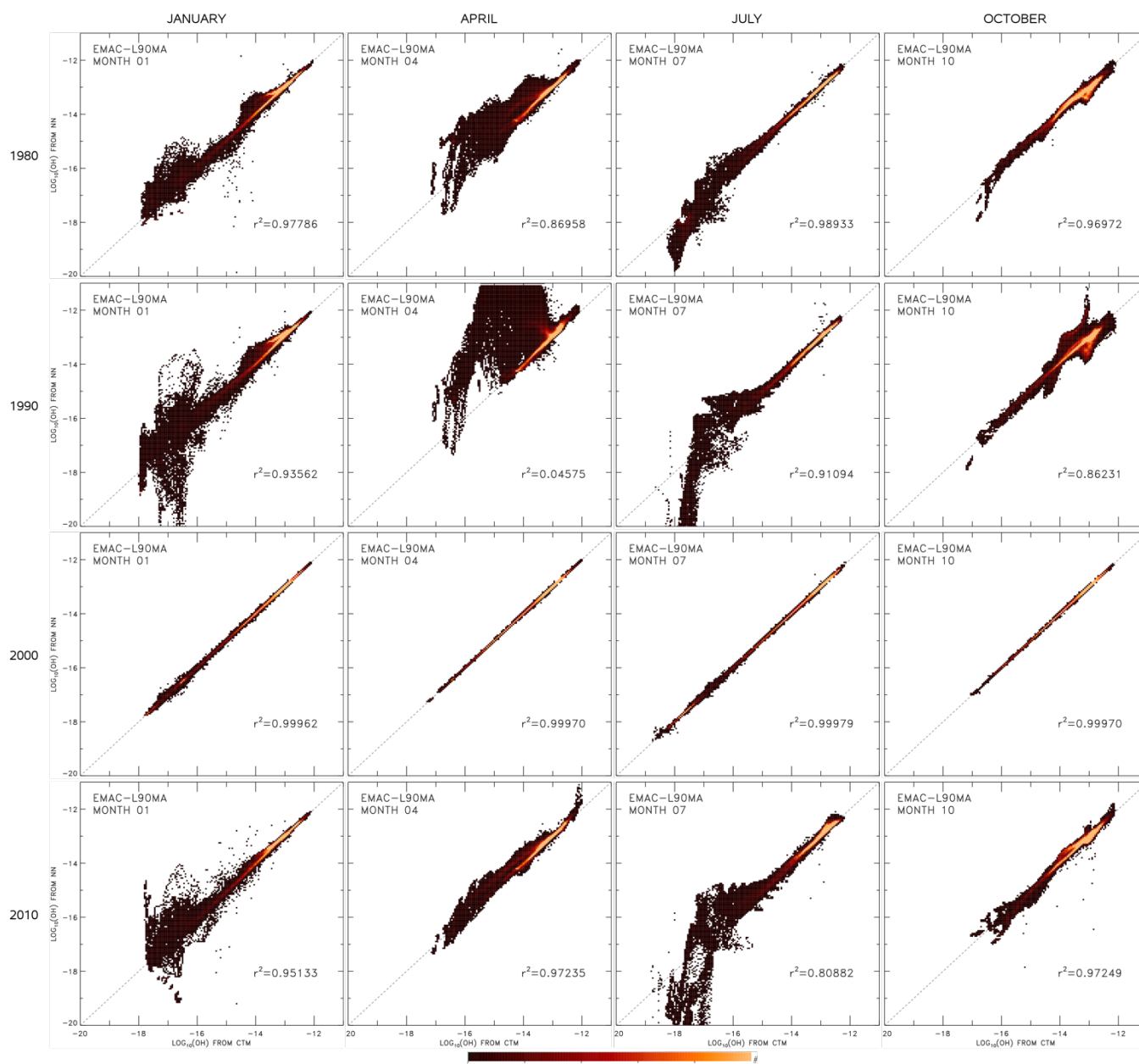
Figure S18. As in Figure S16, but for the REF-C1SD simulation of the EMAC-L90MA model.
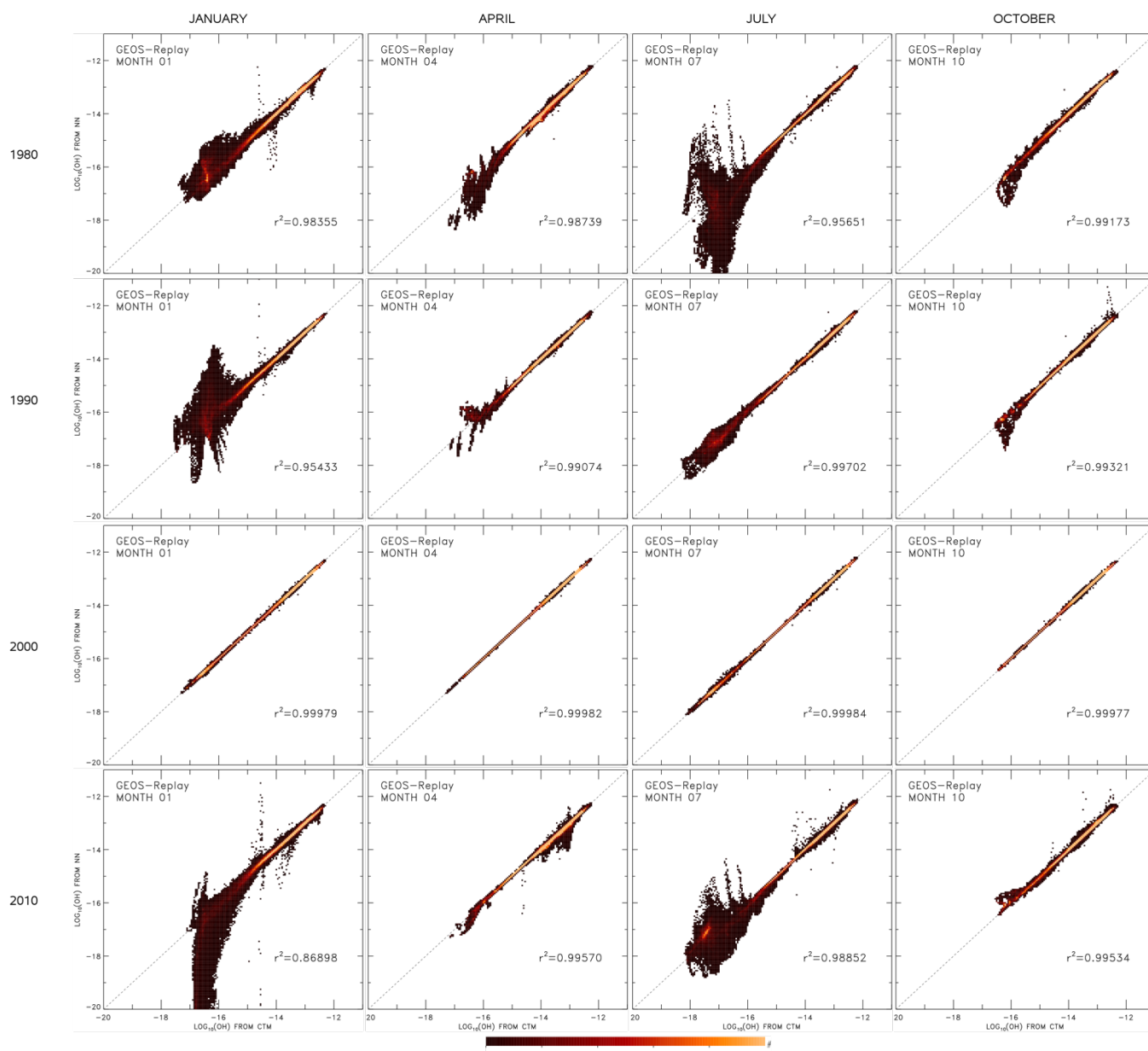
Figure S19. As in Figure S16, but for the REF-C1SD simulation of the GEOS-Replay model.
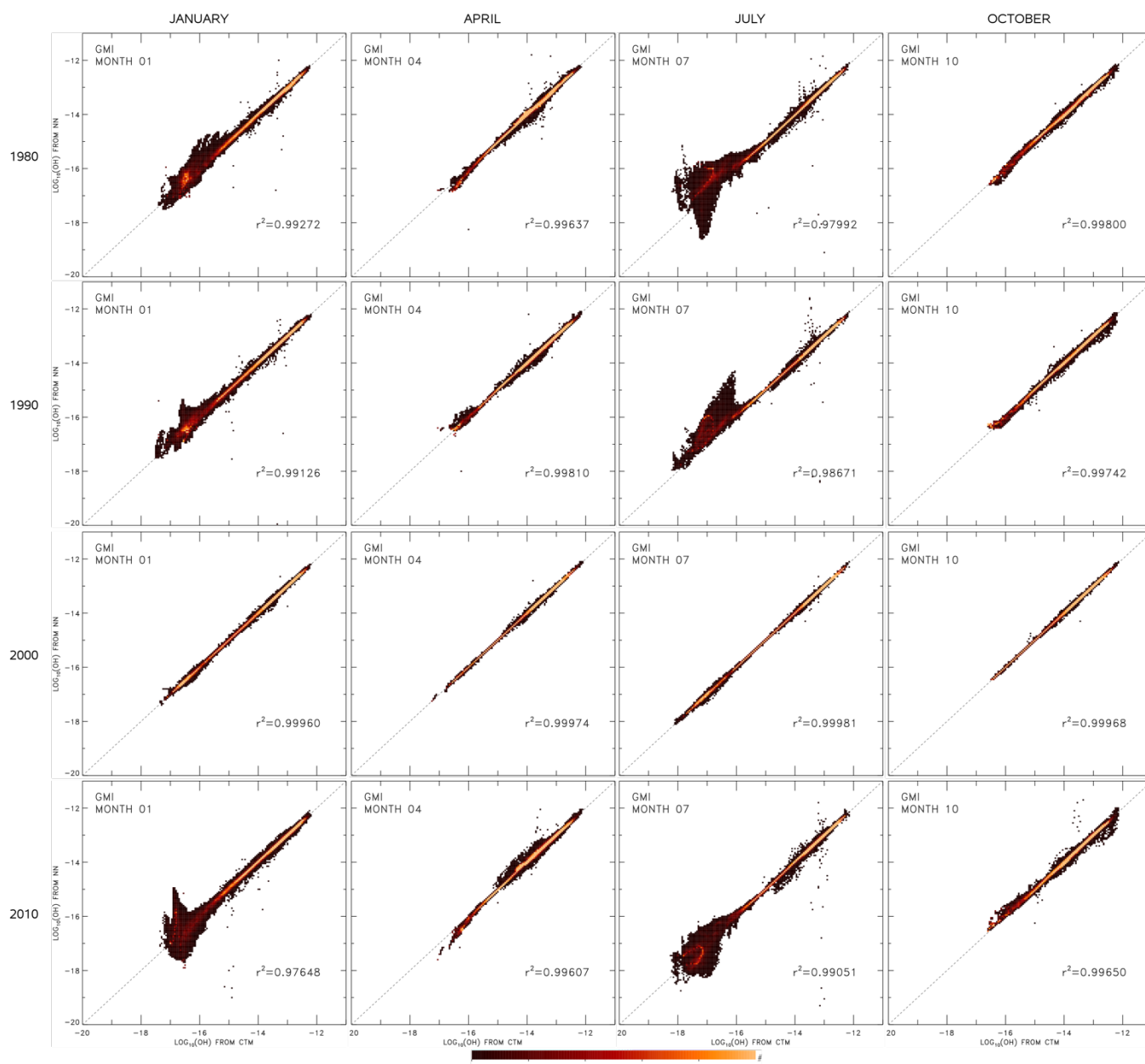
Figure S20. As in Figure S16, but for the REF-C1SD simulation of the GMI model.
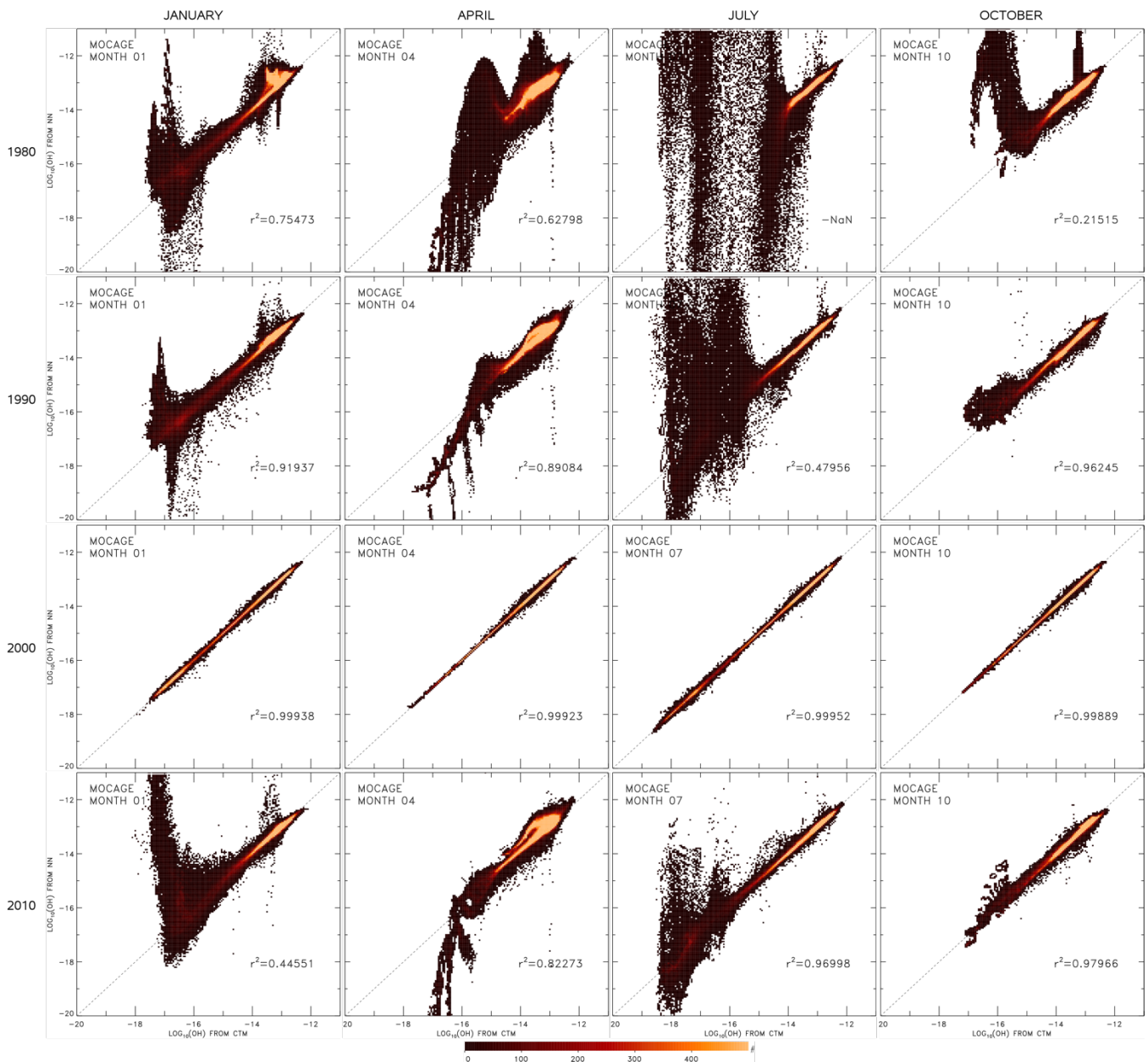
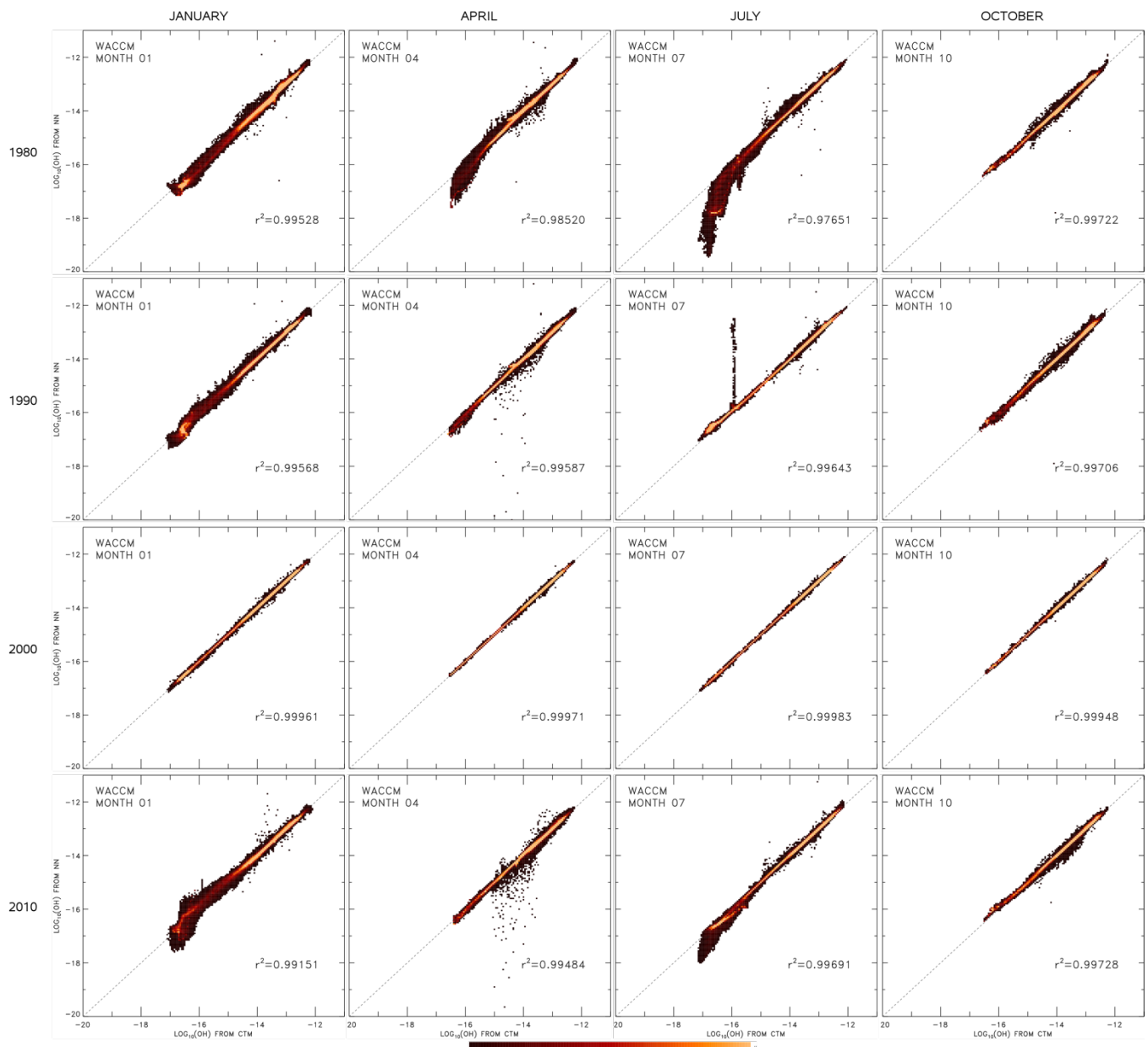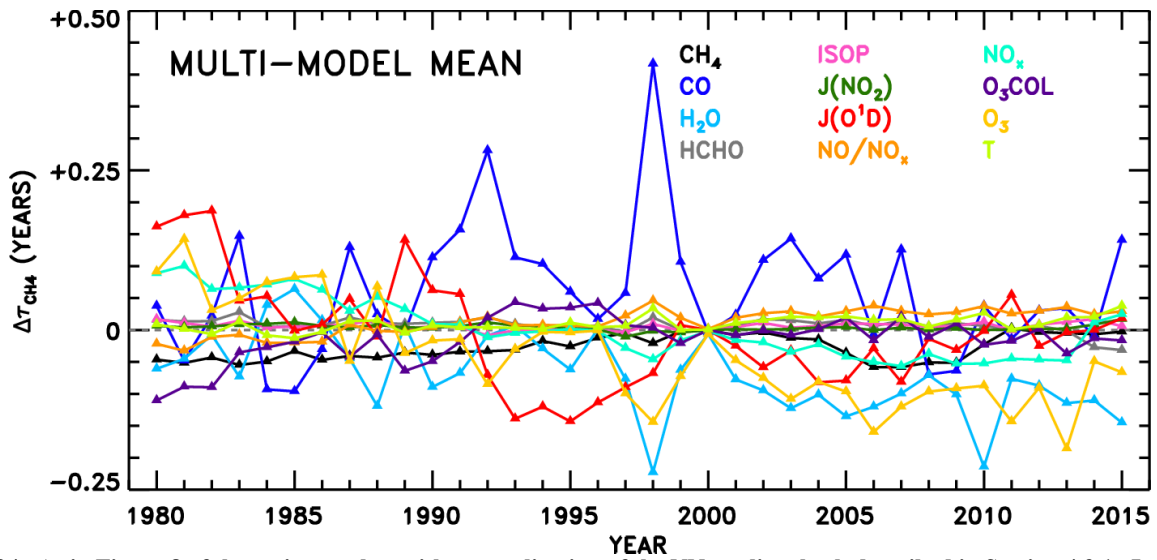**Figure S21.** As in Figure S16, but for the REF-C1SD simulation of the MOCAGE model.
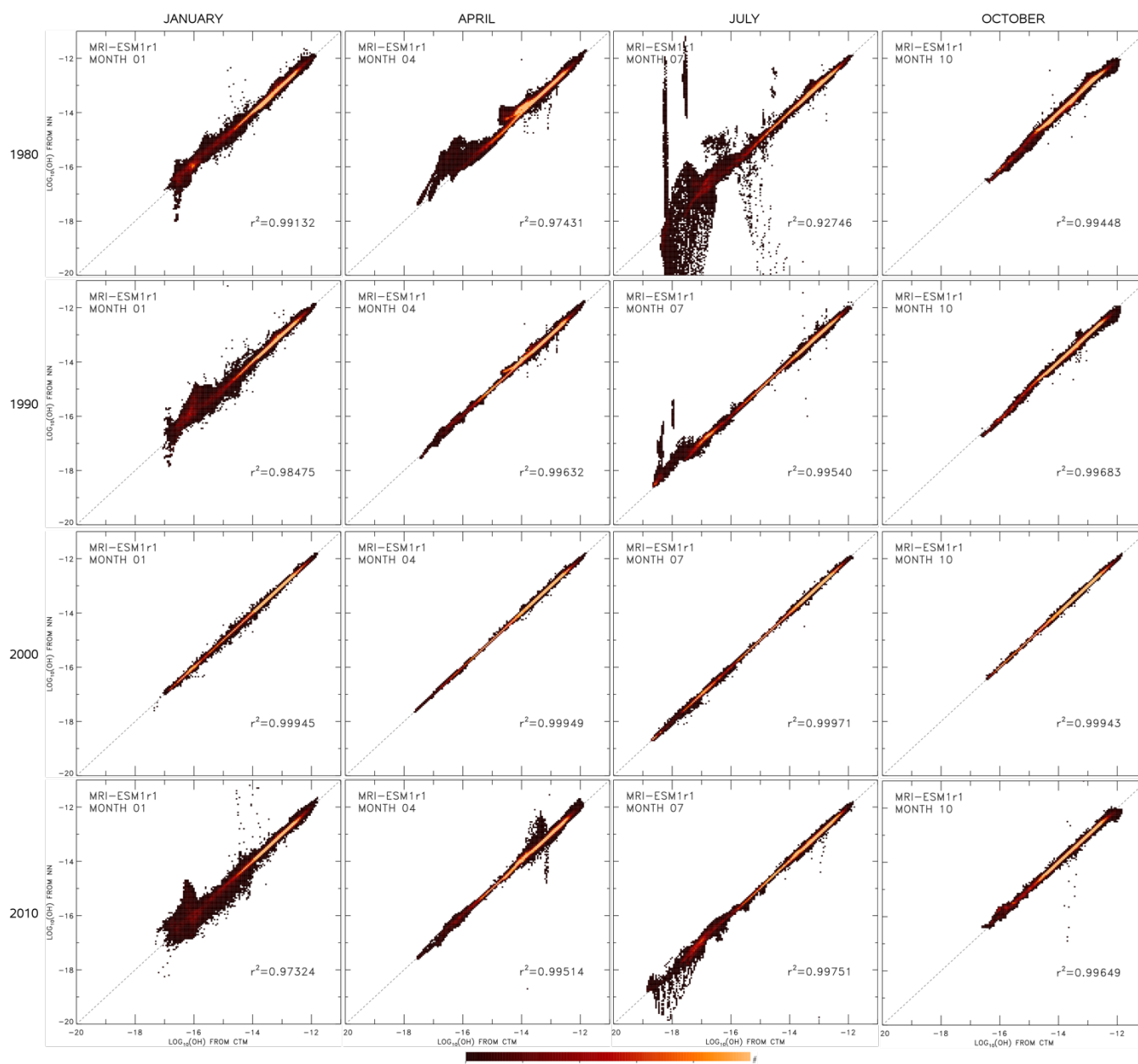
Figure S22. As in Figure S16, but for the REF-C1SD simulation of the MRI-ESM1r1 model.

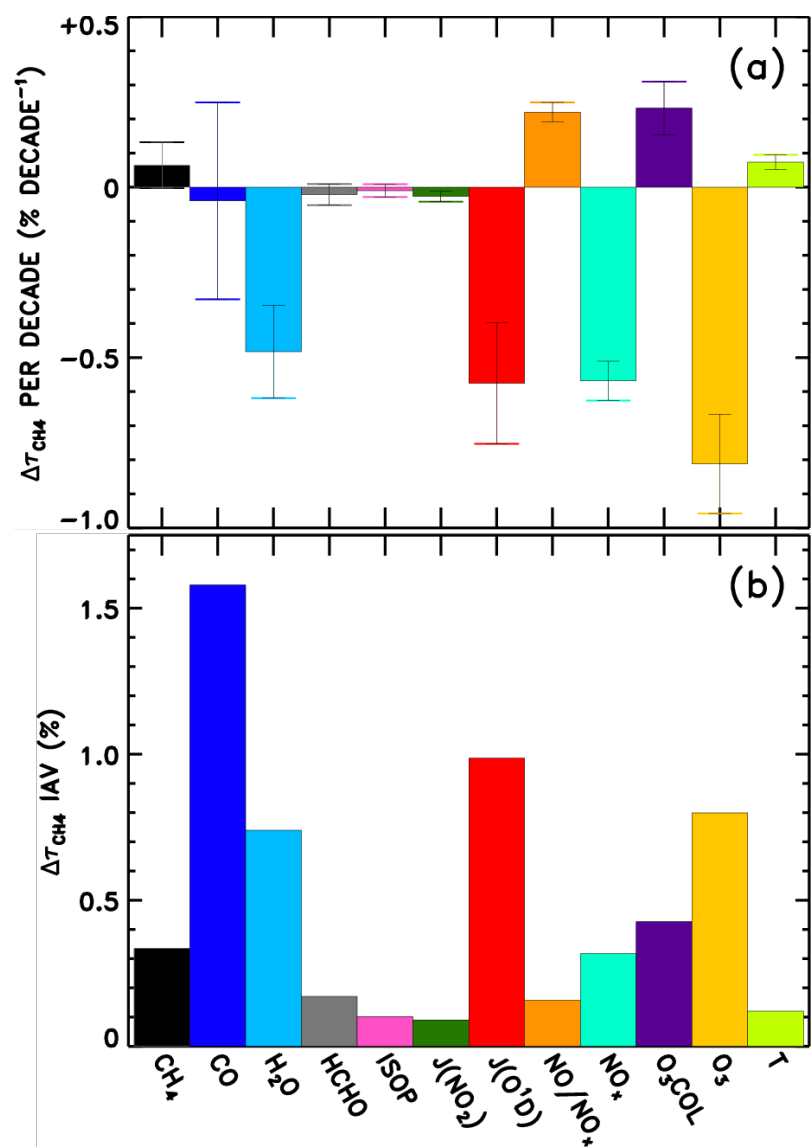**Figure S23. As in Figure S16, but for the REF-C1SD simulation of the WACCM model.**

Figure S24. As in Figure 8 of the main text, but without application of the NN quality check described in Section 4.3.1. In other words, all NN results, from all models and years shown in Fig. 7 of the main text, for the attribution of τ_{CH_4} changes are included in the multi-model mean, except for the three cases that stood out by eye as spurious: EMAC-L47MA CH$_4$, EMAC-L90MA CH$_4$, and MOCAGE O$_3$ COL.

Figure S25. As in Figure 9 of the main text, but without application of the NN quality check described in Section 4.3.1.
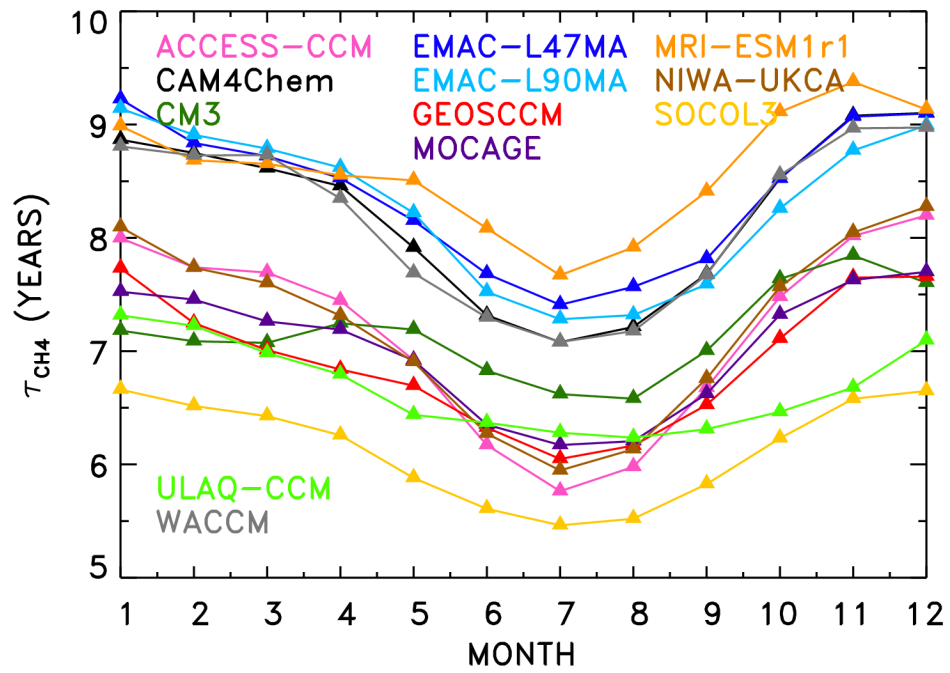
Figure S26. Seasonal variation in CH$_4$ lifetime for year 2000 for the CCMI free-running (REF-C1) model simulations.
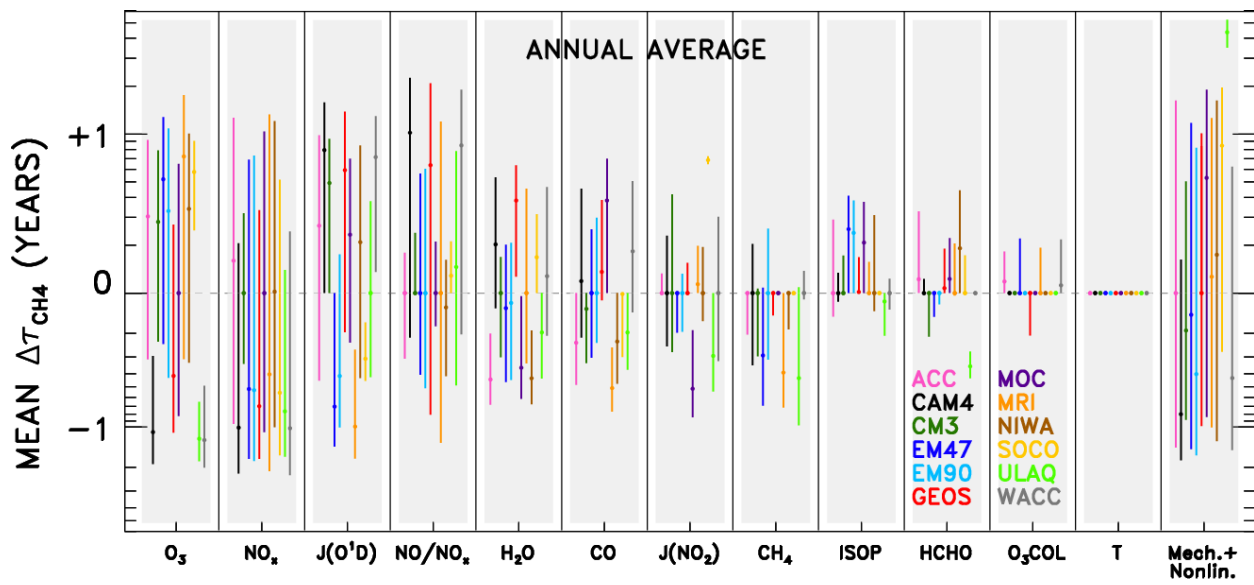
Figure S27. Averaged changes in CH_4 lifetime for the free-running (REF-C1) CCMI simulations. Values of $\Delta\tau_{CH4}$ are accrued for a specified model (color), across all swaps of the indicated variable (x-axis) from all other models. Results are shown annually averaged for year 2000 of the specified dynamics REF-C1SD CCMI and chemical transport model simulations. Circle indicates the mean change in CH_4 lifetime; bars represent the 1σ standard deviation from all model pairings. Variables along the x-axis are ranked by averaged magnitude of the $\Delta\tau_{CH4}$ values (i.e., inputs located farther left are responsible for larger differences in CH_4 lifetime), except for the "Mech.+Nonlin." term, which is shown last to indicate its role as a remainder term.

Specified Dynamics, REF-C1SD

(a)

Free-running, REF-C1

(b)

$J(NO_2)$, 10^{-3} s^{-1}

0   3   6   9   12
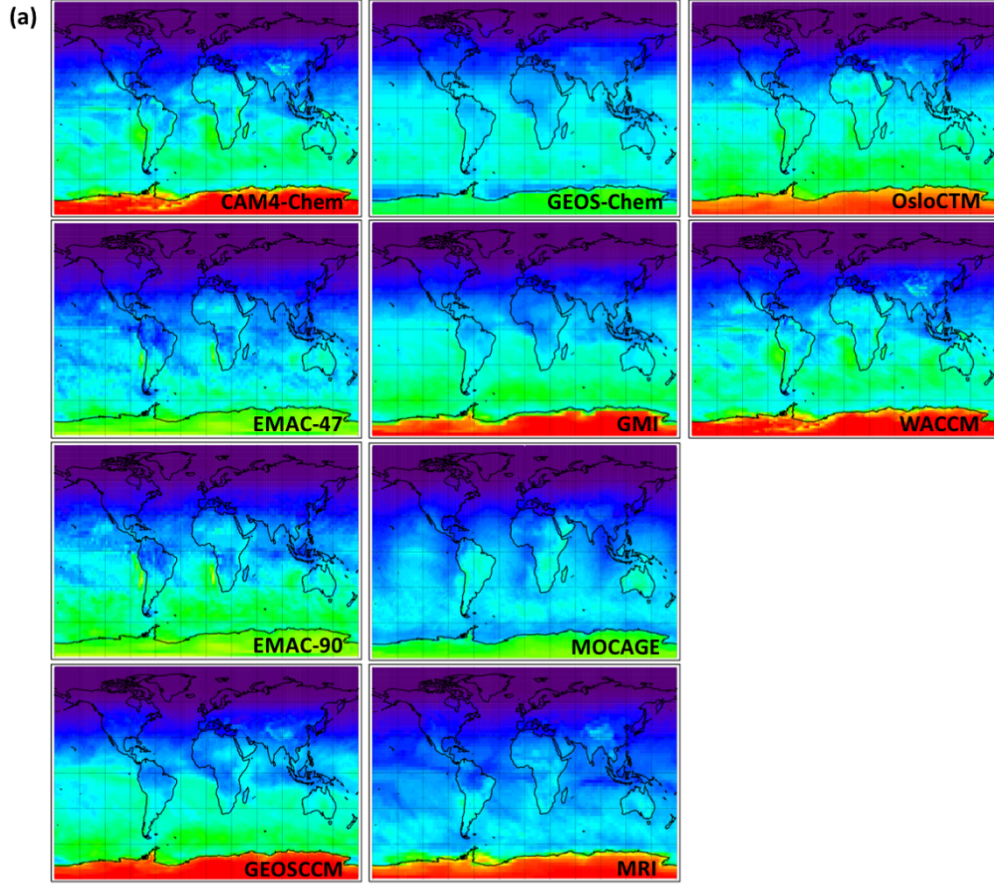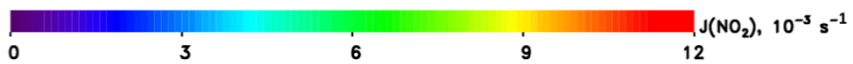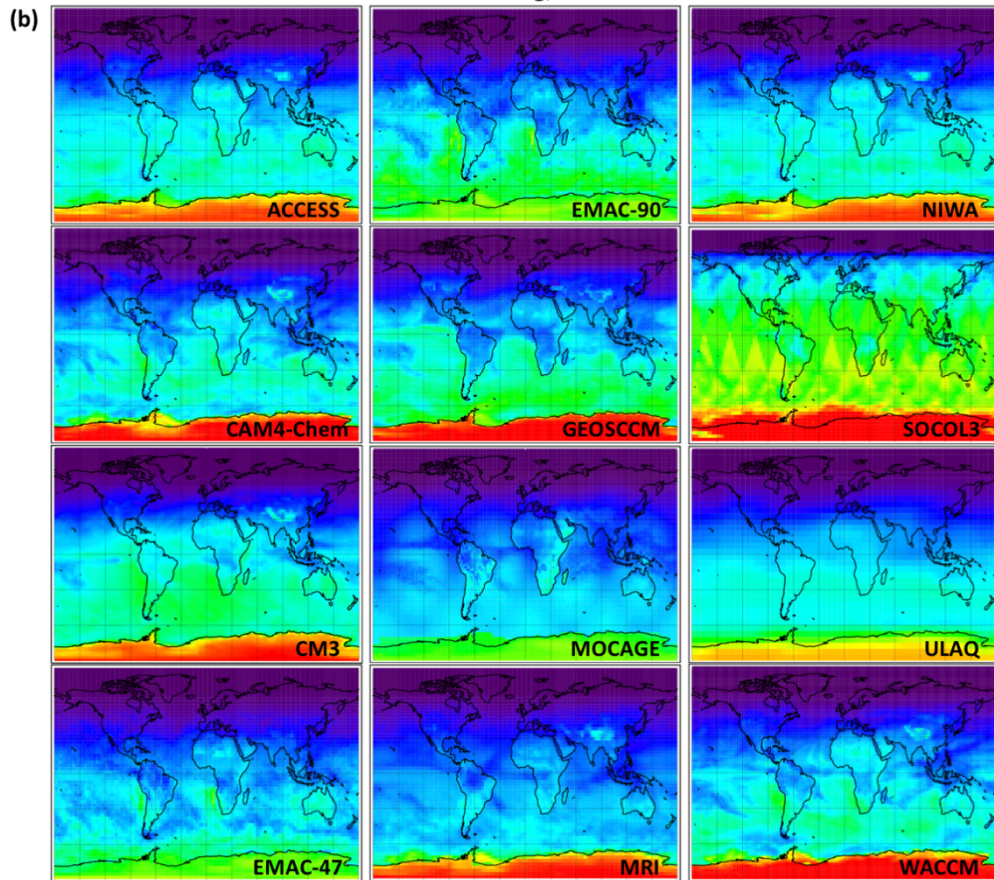
Figure S28. JNO$_2$ values directly from each model at the pressure level closest to 850 hPa for January, 2000 of (a) the REF-C1SD simulations and (b) the REF-C1 simulations.